Observational and modelling analysis of Canada's only F5/EF5 tornado

Chun-Chih Wang[1], John Hanesiak[1], Justin J. Hobson[2], and Mateusz Taszarek[3]

[1]University of Manitoba
[2]Environment and Climate Chanage Canada
[3]Adam Mickiewicz University

November 22, 2023

Abstract

Canada's first and only F5/EF5 tornado associated with a supercell touched down near Elie, Manitoba in the late afternoon of 22 June 2007. An observational and numerical simulation analysis with the Weather Research and Forecasting (WRF) model was undertaken to characterize the pre-storm environment and processes leading to storm initiation. WRF sufficiently reproduced the synoptic and mesoscale features, including a supercell-like storm in the region of interest, and supplemented available observations. Synthesis of observational and simulation data suggests that the environment near Elie immediately before storm initiation was primed for tornadic supercells, with large most-unstable and mixed-layer convective available potential energy (4000 J kg^-1) and sufficient vertical shear (effective bulk wind shear 40 kt; effective storm-relative helicity >200 m2 s^-2). Despite enhancement owing to a cold pool left behind by passing early-afternoon convection, shear remained weaker than those typically found in other North American significant tornadic supercell events. The interaction between a surface trough and convective boundary-layer thermals was the primary triggering mechanism of the Elie supercell. The former appeared to be associated with a low pressure arising from the juxtaposition of lower-troposphere cyclonic differential vorticity advection and lee troughing over the western Red River Valley. More observational analysis and numerical sensitivity experiments are required to better diagnose Manitoba terrain's contribution to the Elie supercell initiation.

Journal of Geophysical Research: Atmospheres

Supporting Information for

Observational and modelling analysis of Canada's only F5/EF5 tornado

C.-C. Wang[1], J. Hanesiak[1], J. J. Hobson[2], and M. Taszarek[3]

1. Centre for Earth Observation Science, Department of Environment and Geography, University of Manitoba, Winnipeg, MB

2. Environment and Climate Change Canada, Victoria, BC

3. Department of Meteorology and Climatology, Adam Mickiewicz University, Poznan, Poland

Contents of this file

Movie S1
Unpublished manuscript S1

Additional Supporting Information (Files uploaded separately)

Caption for Movie S1: An animation of the observed radar reflectivity (filled; left panel), and radial velocity (filled; right panel) at the 0.5 elevation angle between 2000 UTC 22 June 2007 and 0000 UTC 23 June 2007. Elie, MB is indicated by a purple dot. Station models in the area are also displayed. Thick circles indicate the 50- and 100-km range rings, with the altitude (km ASL) at these ranges indicated in the boxes.

Introduction

An animation was created using the same software and data used to produce Figure 5 in the manuscript. The purpose of this supplemental information is to help readers see the radar-detected flow evolution around the time of the Elie supercell initiation when it is animated. This animation is referenced in section 3.3.1 of the manuscript.

Some analysis in the submitted manuscript (in section 5.1.1) was based on the results of an unpublished manuscript by J. Hanesiak, M. Taszarek, D. Walker, C.-C. Wang, and D. Betancourt "**Significant tornado environments in Canada using ERA5-derived convective parameters**", submitted to the Journal of Weather and Climate Extremes in April 2023 and is currently in revision. This unpublished manuscript was also referenced in various sections throughout this submitted manuscript.

Observational and modelling analysis of Canada's only F5/EF5 tornado

C.-C. Wang[1], J. Hanesiak[1*], J. J. Hobson[2], and M. Taszarek[3]

[1]Centre for Earth Observation Science, Department of Environment and Geography, University of Manitoba, Winnipeg, MB
[2]Environment and Climate Change Canada, Victoria, BC
[3]Department of Meteorology and Climatology, Adam Mickiewicz University, Poznan, Poland

Key Points:

- Weather observations and numerical simulations were used to diagnose the pre-storm environment and triggering of the Elie, Manitoba tornado.
- Pre-storm conditions were found favorable for tornadic supercells; enhanced by the interaction between a remnant cold pool and ambient flow.
- The interaction between a trough and boundary-layer thermals was the primary triggering mechanism of the Elie, Manitoba tornadic supercell.

*Wallace Building, 125 Dysart Rd., University of Manitoba, Winnipeg, Manitoba, Canada, R3T 2N2

Corresponding author: John Hanesiak, john.hanesiak@umanitoba.ca

Abstract

Canada's first and only F5/EF5 tornado associated with a supercell touched down near Elie, Manitoba in the late afternoon of 22 June 2007. An observational and numerical simulation analysis with the Weather Research and Forecasting (WRF) model was undertaken to characterize the pre-storm environment and processes leading to storm initiation. WRF sufficiently reproduced the synoptic and mesoscale features, including a supercell-like storm in the region of interest, and supplemented available observations. Synthesis of observational and simulation data suggests that the environment near Elie immediately before storm initiation was primed for tornadic supercells, with large most-unstable and mixed-layer convective available potential energy (> 4000 J kg^{-1}) and sufficient vertical shear (effective bulk wind shear $\sim$ 40 kt; effective storm-relative helicity $>$ 200 m^2 s^{-2}). Despite enhancement owing to a cold pool left behind by passing early-afternoon convection, shear remained weaker than those typically found in other North American significant tornadic supercell events. The interaction between a surface trough and convective boundary-layer thermals was the primary triggering mechanism of the Elie supercell. The former appeared to be associated with a low pressure arising from the juxtaposition of lower-troposphere cyclonic differential vorticity advection and lee troughing over the western Red River Valley. More observational analysis and numerical sensitivity experiments are required to better diagnose Manitoba terrain's contribution to the Elie supercell initiation.

Plain Language Summary

A severe thunderstorm produced the strongest tornado ever recorded in Canada on 22 June 2007 that struck Elie, Manitoba, Canada. To better understand and characterize the conditions leading to the storm, weather observations and the data produced by a specialized computer model were analyzed. We found that the conditions were overall favorable for the formation of severe thunderstorms that would produce tornadoes. These conditions were enhanced by a cluster of showers that passed over the area in the early afternoon. An external lifting mechanism was also required to initiate the storm, which we attributed to the combined lift associated with a surface air mass boundary and updrafts that formed due to daytime solar heating. The air mass boundary may have been associated with a low pressure system resulting from airflow interacting with the shallow western Manitoba terrain. Additional observational analysis and computer modelling experiments are needed to gain further insights into the effects of Manitoba's terrain on the formation of the Elie, Manitoba tornadic thunderstorm.

1 Introduction

Although not as well-known as the U.S. for significant tornado events, Canada has experienced several notable modern-day tornado disasters including the 1985 Barrie tornado (Etkin et al., 2002), the 1987 Edmonton tornado (Bullas & Wallace, 1988; Charlton et al., 1995), and the 2000 Pine Lake tornado (Joe & Dudley, 2000; Erfani et al., 2003). These events caused property damage ranging from a few to hundreds of millions of CAD, with fatalities as many as 30 and injuries as many as 300. Therefore, it is in the public's interest to better understand Canadian tornado environments to improve knowledge gaps and prediction of such events. Such is one of the goals of the Northern Tornadoes Project (NTP; Sills et al., 2020), which was established in 2017 to focus on improving the detection and documentation of Canadian tornadoes using various existing and new data sources and technologies.

As part of NTP science, we present a meteorological analysis of the Elie, Manitoba F5 tornado that occurred on 22 June 2007. This event deserves a detailed case study since it is still the strongest tornado in Canada, and has several unresolved questions about its formation and evolution. The tornado occurred between 2320 UTC 22 June 2007 to

0000 UTC 23 June 2007 (CDT=UTC-5). It was narrow ($\sim$ 200 m wide) and slow-moving (i.e., traveling at ~ 2 m s^{-1}; Hobson (2011)), wiping several houses off their foundation and tossing a cargo van along its path. It was rated F5 in the final damage assessment report, which was rather unusual given its narrow width (Brooks, 2004), and was still rated five on the Enhanced Fujita (EF) scale (MacDonald et al., 2004) after Canada adopted the scale in 2013. The full damage survey, rating process, and estimated path of this tornado can be found in McCarthy et al. (2008).

Because of its uniqueness among the documented Canadian tornadoes, an examination of what the environment was like prior to storm initiation and what the storm-triggering mechanisms were, is warranted. Key tornadic supercell environmental ingredients include large conditional instability and low-level moisture, which are indicated by convective available potential energy (CAPE; e.g., Maddox, 1976; Brooks et al., 1994; R. L. Thompson et al., 2003, 2004a) and strong vertical wind shear, measured by bulk wind shear (or bulk wind difference; BWD) and/or storm-relative helicity (SRH; e.g., Johns & Doswell III, 1992; Johns et al., 1993; E. N. Rasmussen & Blanchard, 1998; Markowski et al., 2003; R. L. Thompson et al., 2003). Low-level triggers of any deep moist convection can be in the form of mesoscale boundaries (and their interactions) as well as synoptic-scale systems such as warm and cold fronts (e.g., Kingsmill, 1995; Koch & Ray, 1997; Ziegler & Rasmussen, 1998; Weckwerth & Parsons, 2005; Wakimoto & Murphey, 2010; Wang & Kirshbaum, 2015; Wilson et al., 2018). Some observational studies have shown that boundaries can also modify the local wind pattern and lead to more favorable conditions for tornadoes (e.g., Maddox et al., 1980; Sills & King, 2000; Giaiotti & Stel, 2007; Taszarek et al., 2016; Pilguj et al., 2019).

In this work we offer a subsequent opportunity to compare the Elie event to other significant tornado cases in Canada and the U.S. due to its significance in the nation's tornado history. Studies of tornado environments based on historical events in the U.S. have been extensive (e.g., E. N. Rasmussen & Blanchard, 1998; Brooks et al., 2003; R. L. Thompson et al., 2003, 2007, 2012), with only limited work done in Canada. In Canada, Dupilka and Reuter (2006b) and Dupilka and Reuter (2006a) studied Alberta's severe thunderstorm environments during a handful of cases, including those that were tornadic. Hanesiak et al. (2023) recently compared the storm environments during significant tornado (F2/EF2+) events in different provinces across Canada.

As a witness to the tornado's entire life cycle, J. Hobson was the first to conduct an observational analysis and comparison of the Elie event to a few other significant tornado events in the U.S. and Canada (see Hobson (2011)). However, due to the lack of meteorological observations immediately before the supercell initiation, the full mesoscale environment and the physical mechanisms of the storm trigger(s) remain inadequately understood.

Building on Hobson (2011), the present study will utilize a numerical weather prediction (NWP) model to obtain the three-dimensional flow evolution during the Elie event. Numerical simulations have been used in many studies of notable tornado events around the world (e.g., Litta et al., 2010, 2012; Matsangouras et al., 2011, 2016; Taszarek et al., 2016; Miglietta et al., 2017; Pilguj et al., 2022). These studies successfully reproduced the observed synoptic and mesoscale flow and severe convection development to a reasonable degree using $\mathcal{O}(1)$ km model grid spacings. Observational-modelling studies of Canadian events have been limited. A few exceptions include Erfani et al. (2003), who found that ascent and moisture transport associated with a mountain-plain circulation, coupled with deep-layer shear and destabilization ahead of an upper-level trough, led to the Pine Lake, Alberta tornadic supercell. Bisson and Paola (2000) found that the late-day low-level jet development over southern Manitoba created sufficient low-level shear to produce the 2000 Brunkild, Manitoba tornadic supercell in an otherwise suboptimal environment featuring only large conditional instability.

The objective of the present study is to identify and characterize the synoptic and mesoscale features that contributed to producing the Elie tornadic supercell using all available observations and model simulations. This study will lay the groundwork for future case studies of other Canadian significant tornado events, with the goal of improving the understanding of their environments and physical mechanisms. The paper layout is as follows: section 2 describes the observational datasets and numerical simulation setups. Observational analyses of the pre-storm environment and storm evolution are shown in section 3. Section 4 evaluates the model performance against available and proxy observations. Section 5 presents the analyses of the simulated flow immediately before the supercell initiation. The findings are summarized in section 6.

2 Data and Methods

2.1 Observational datasets

2.1.1 The study area

The topography of south-central Manitoba is characterized by the relatively flat croplands in the Red River Valley (RRV hereafter; Fig. 1). The provincial capital, Winnipeg, is situated near the valley base (elevation $\sim$ 230 m above sea level, ASL), with Elie located about 40 km to the west of the city. Two large, south-north-oriented lakes, Lakes Winnipeg and Manitoba, lay $\sim$ 60 km to the north-northeast and $\sim$ 80 km to the northwest of Winnipeg, respectively. Lake breezes frequently occur during the summer along the lake shores (Curry, 2015), with their frontal updrafts having the potential to trigger deep moist convection.

The western slope of the RRV features taller terrain than its eastern slope, with the Porcupine Hills, Duck Mountain, and Riding Mountain, west of the RRV. Each mountain complex rises to 600-800 m ASL (or 400-600 m from the valley base). Manitoba terrain generally has been thought to have limited impacts on the regional convection pattern due to its shallowness (Erfani, 1999).

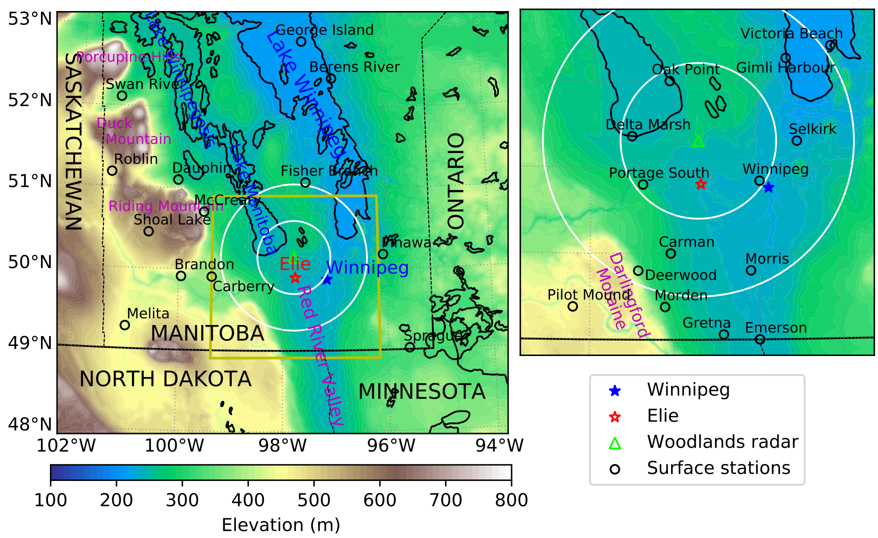

Figure 1. Elevation maps (based on the 2-min U.S. Geological Survey topography data used in the WRF simulation) of southern Manitoba and locations where surface station data was available. The right panel shows the zoomed-in area within the yellow box in the left panel. The white circles denote the 50- and 100-km Woodlands, MB radar range rings.

2.1.2 Radar

The Environment and Climate Change Canada's (ECCC), 5-cm, C-band Doppler operational weather radar at Woodlands, MB provided radar coverage for much of south-central Manitoba (Fig. 1). 10-min scans of reflectivity and radial velocity at the 0.5° elevation angle between 1500 UTC 22 June 2007 to 0200 UTC 23 June 2007 were used in this study. These fields have 0.5° azimuthal and 0.5 km radial resolutions and a maximum range of about 113 km from the radar. Radar signals can be contaminated by ground clutter, velocity aliasing, or other artifacts such as dual pulse repetition frequency velocity errors (Joe & May, 2003; Fabry, 2015). ECCC filtered out ground clutter from the reflectivity data and unfolded the radial velocity up to 48 m s^{-1}. To eliminate spurious noise in the velocity data, a 3-by-3 median filter like that implemented in Mahalik et al. (2019) was applied. Although volumetric scans were also available from this radar, they were not used because they were too noisy and did not provide any additional insight into identifying the storm-triggering mechanism(s). The volumetric data were not used to investigate the 3D storm structure since this is beyond the scope of this paper.

2.1.3 Satellite

The visible channel imagery from the National Oceanographic and Atmospheric Administration's (NOAA) Geostationary Operational Environmental Satellite (GOES) 12 was examined to identify the presence of any shallow cumulus field where the low-level lift is locally enhanced, which may indicate a low-level mesoscale boundary (Purdom, 1976; Sills et al., 2011; Alexander et al., 2018). In this study, the satellite images produced by NOAA between 2000 UTC 22 June 2007 and 0000 UTC 23 June 2007 were used.

2.1.4 Sounding

The closest operational rawinsonde observations are International Falls, MN, and Bismarck, ND. However, both are ~ 400 km away from Elie, thus the environment sampled there might not be representative. Fortunately, the Prairie and Arctic Storm Prediction Centre (PASPC) released a special sounding from Winnipeg (XWI) at 1800 UTC of the Elie, MB tornado day (22 June 2007). Air temperature, relative humidity, pressure, wind, and height profiles were sampled.

2.1.5 Surface stations

Hourly surface observations at 27 stations in the southern half of Manitoba (south of 53°N) were used to diagnose the regional surface weather conditions before storm initiation between 1200 UTC and 2100 UTC 22 June 2007 (Fig. 1). Most of these stations were standard automated weather stations at airports that collected quality-controlled surface air temperature, dew point, pressure, wind speed, and wind direction. A few were temporary stations used in other field studies that no longer operate today (e.g., Delta Marsh) or private stations installed by the local farmers (e.g., Morris). All fields are assumed taken at the standard heights above ground level (2 m AGL for temperature, dew point, and pressure; 10 m AGL for wind).

2.2 WRF simulation setup

The Weather Research and Forecasting (WRF) model version 4.2.1 (Skamarock et al., 2019) was used to simulate the three-dimensional synoptic and mesoscale flows during the Elie tornado event. The Runge-Kutta 3rd-order scheme was used to integrate the model's 3D moist atmospheric equations in time, with horizontal and vertical advection computed by 5th- and 3rd-order schemes, respectively. The scalar advection is positive-definite. The 6-hourly, 0.5° resolution Global Forecasting System (GFS) model analyses were used to initialize the simulation and update the lateral boundary conditions. The model was integrated for 18 hr starting at 1200 UTC 22 June 2007 to capture the morning to late evening periods.

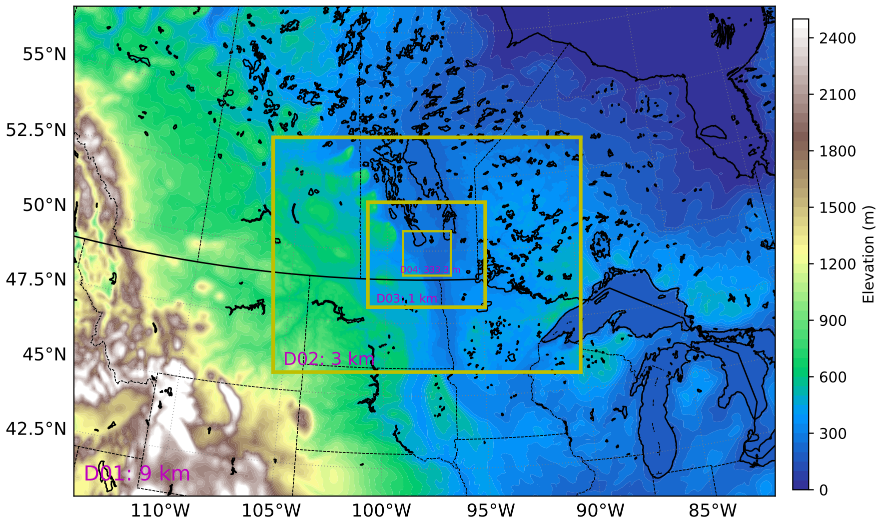

Figure 2. The WRF simulation domains (the nested domains are represented by the boxed regions) with the terrain elevation indicated in filled contours.

Four, two-way nested domains (D01-D04) were used in the simulation (Fig. 2), with horizontal grid spacings $\Delta\ x = \Delta\ y$ decreasing from 9 km, 3 km, 1 km, to 333.3 m, respectively. A similar grid-spacing configuration had been used in other numerical investigations of tornadic supercells (e.g., Pilguj et al., 2019). The inclusion of the sub-kilometer D04 was intended to resolve large intracloud eddies (Bryan et al., 2003), lake breeze fronts, which are similar to sea breeze fronts (Lyons & Olsson, 1973; Chiba, 1993; Wood et al., 1999; Curry et al., 2016), and other boundary layer drafts such as thermals and horizontal convective rolls (Balaji & Clark, 1998; Weckwerth et al., 1997; Dailey & Fovell, 1999; Bryan et al., 2003). A hybrid vertical coordinate was used in that the model levels are roughly terrain-following at the ground and gradually relax to isobaric at upper troposphere. 115 user-specified model levels were used up to 50 hPa, yielding a nominal vertical resolution of ~ 30 m in the lowest 1 km and the lowest de-staggered level at ~ 20 m above the ground. A rigid boundary caps the model top with an implicit gravity wave damping layer specified in the uppermost 5 km to prevent spurious wave reflections.

Long- and short-wave radiation were parameterized using the Rapid Radiative Transfer Model for Global Climate Models (RRTM-G) schemes. Land surface processes were modeled using the Noah land surface scheme. A Smagorinsky-type closure was used to represent horizontal turbulent mixing, whereas vertical mixing was handled by the Mellor-Yamada-Janjic (MYJ) planetary boundary layer (PBL) scheme. The surface layer was parameterized using the Janjic scheme based on the Monin-Obukhov similarity theory and Zilitinkevich thermal roughness length. A sensitivity experiment by varying the PBL-surface layer scheme pairs, namely the Yonsei University, quasi-normal scale elimination (QNSE), Mellor-Yamada Nakanishi and Niino, and Shin-Hong schemes, was also conducted. The Thompson graupel scheme was chosen to parametrize the microphysics, with the cloud droplet concentration set to the typical continental value of 300 cm^{-3} according to the scheme's recommendation. The Grell-Freitas cumulus parameterization was used for the 9-km resolution domain (D01) only.

As mentioned, Manitoba lakes frequently generate lake breezes during summer. Because lake breezes are driven by the land-water temperature contrast (Lyons, 1972; Crosman & Horel, 2012), the proper initialization of the lake surface temperatures (T_{lake}) in the WRF simulation is crucial to reasonably capture lake effects. T_{lake} was initialized using the daily-averaged surface air temperature using the 6-hourly GFS analyses between 0000 UTC and 1800 UTC 22 June 2007. This was done because the lakes in Manitoba are either too small or narrow ($< 0.5°$ latitudinally or longitudinally) to be resolved in the 0.5° resolution GFS analyses, introducing the potential for WRF to poorly initialize T_{lake} (readers are referred to Chapter 3-27 of the WRF Users' Guide: `https://www2.mmm.ucar.edu/wrf/users/docs/user_guide_v4/v4.2/WRFUsersGuide_v42.pdf` for a detailed explanation of this issue). The comparison of T_{lake} in Manitoba initialized with this approach vs. those without against the National Aeronautics and Space Administration (NASA)'s Group for High-Resolution Sea Surface Temperature (GHRSST; `https://worldview.earthdata.nasa.gov/`) dataset values on 22 June 2007 shows that the former were generally within 2°C of the GHRSST values, whereas the latter were about 10°C too cold. Therefore, the surface air temperature-initialized T_{lake} was reasonable and was fixed throughout the simulation.

3 Event Overview

3.1 Large-scale pattern

The hourly, fifth-generation European Centre for Medium-Range Weather Forecasts reanalysis (ERA5; Hersbach et al., 2020) was used to examine the regional synoptic-scale flow on 22 June 2007. ERA5 has been found to reasonably depict observed weather patterns and convective environments in various parts of the world (e.g., Balsamo et al., 2018; Coffer et al., 2020; F. Li et al., 2020; Taszarek et al., 2021; Pilguj et al., 2022). The 20-km Rapid Update Cycle (RUC) model analysis was also examined as additional supporting data. Both datasets showed similar diurnal evolution of large-scale patterns, therefore, only the ERA5 is discussed.

The Elie event featured a broad upper-level ridge above 500 hPa over the Canadian Prairies (Fig. 3a, b), with no significant diffluence and jet streak influences at 200 hPa or vorticity advection at 500 hPa. Thus, very little to no upper-level (500 hPa or above) forcing for vertical motion was present before storm initiation.

At 850 (700) hPa, 20-25 kt southwesterly (west-northwesterly) at 220° (290°) winds advected warm air into southern Manitoba behind a shortwave trough moving eastward across northern Manitoba in the morning (Figs. 3c-f), with associated isolated precipitation passing over the RRV (not shown). The warm air advection (WAA) partly contributed to the stout 900-700 hPa capping inversion in the 1800 UTC XWI sounding (Fig. 4a). Analysis of 850-700 hPa vorticity advection reveals that anti-cyclonic vorticity advection (AVA) with height existed over southern Manitoba until 1900 UTC, favoring large-scale subsidence and mid-level capping (Fig. 3c). Differential vorticity advection flipped to cyclonic across the 850-700 hPa layer by 2100 UTC, leading to forcing for ascent (Fig. 3d). Cyclonic differential vorticity advection, solar heating, and low-level warm air and moisture advection following an early-morning warm frontal passage (Figs. 3g, h) were likely the dominant mechanisms of lower-troposphere lift and destabilization in the afternoon over southern Manitoba.

By 2100 UTC, the warm front's parent low pressure was approaching the Elie area from the north along with its associated cold front. Southern Manitoba was situated within the warm sector of this surface low.

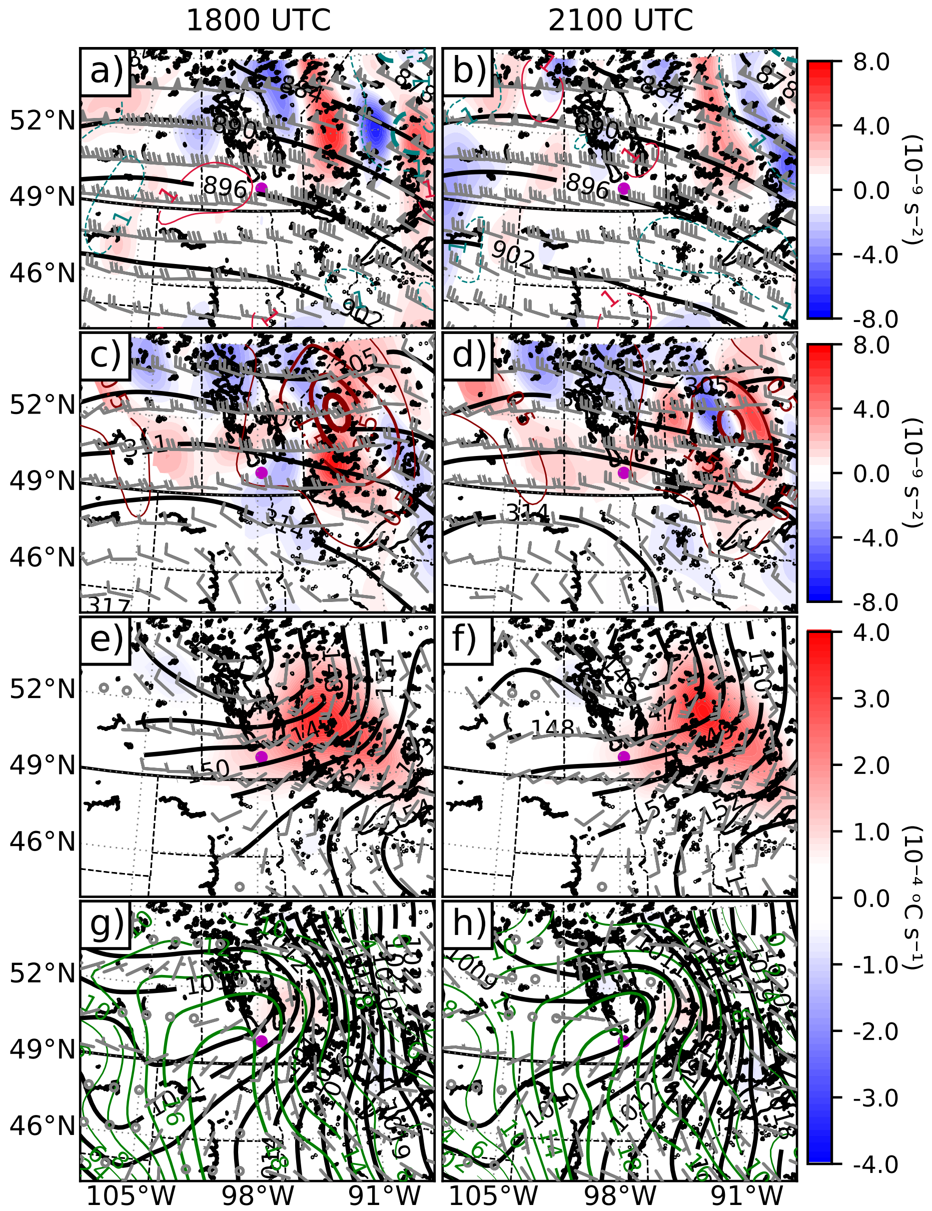

Figure 3. Left column: maps of a) 500-hPa vorticity advection (filled), 200-hPa divergence (10^{-5} s^{-1}), 200 and 500 hPa averaged geopotential heights (black solid; in dm), and wind barbs (full barbs denote 10 kt and half barbs denote 5 kt; all plotted barbs will have this same convention), c) 700-hPa geopotential heights (black solid), temperature advection (10^{-4} °C s^{-1}), the differential absolute vorticity advection between 850-700 hPa (filled), and wind barbs, e) 850-hPa temperature advection (filled), geopotential heights (solid), and wind barbs, and g) surface temperature advection (filled), sea-level pressure (black solid), dew point (green solid; °C), and wind barbs at 1800 UTC 22 June 2007. Right column: the same as in the left column, but for 2100 UTC 22 June 2007.

3.2 Pre-storm initiation environment

CAPE and CIN were computed for the surface-based (SB), lowest 100-mb mixed layer (ML), and lowest 300-mb most-unstable (MU) parcels for the observed XWI sound-

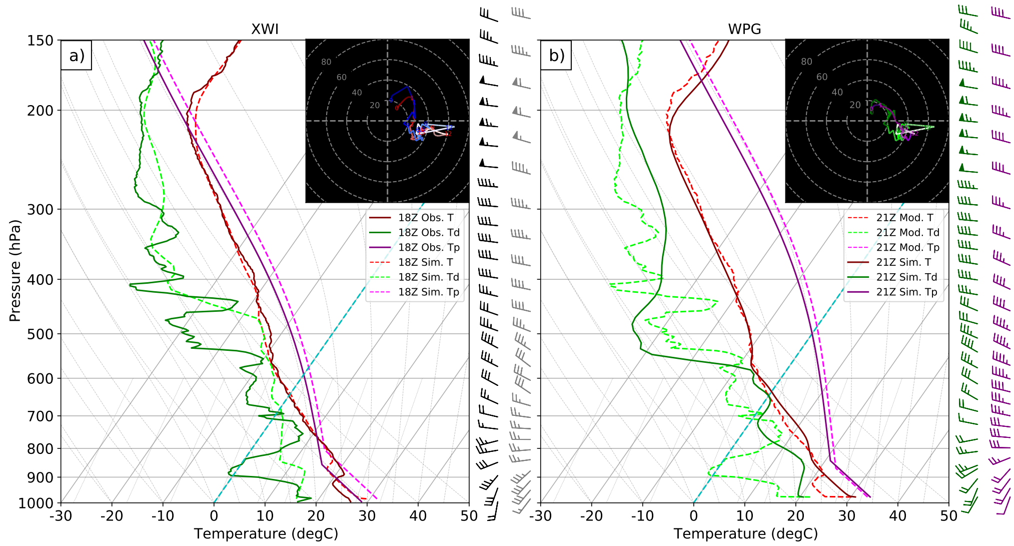

Figure 4. a) Observed and WRF simulated 1800 UTC 22 June 2007 soundings from XWI. The observed wind profile (hodograph) is indicated in black (blue) while the simulated wind profile is indicated in gray (red). b) The modified 1800 UTC XWI (with 2100 UTC WPG surface observations and Woodlands radar VAD winds up to 1.5 km ASL) and simulated soundings at 2100 UTC 22 June 2007 at WPG. The modified wind profile and hodograph are indicated in green while the simulated ones are shown in purple. All parcel temperature profiles are for surface-based parcels.

ing (Table 1). BWD and SRH were calculated for various fixed layers above the ground (0-1 km and 0-6 km for BWD; 0-3 km for SRH), as well as the 'effective' layer (EBWD and ESRH (R. L. Thompson et al., 2007). SRH was obtained using the Bunkers et al. (2014) storm motion of 17 kt (~ 9 m s^{-1}) from 300° derived from the 1800 UTC XWI sounding. Lastly, a lower mixed-layer lifting condensation level (MLLCL) often suggests a higher boundary-layer relative humidity, which prevents strong outflow from forming to cut off storm inflow and increase tornado probability (E. N. Rasmussen & Blanchard, 1998; Markowski et al., 2002). This parameter was also computed. The convective parameters were calculated using SHARPpy (Blumberg et al., 2017).

Previous proximity sounding studies of tornadic supercell environments in North America have found that these storms are typically associated with environmental MLCAPE or MUCAPE > 1000 J kg^{-1}, SBCIN or MLCIN > -50 J kg^{-1}, 0-1 km BWD > 10 kt, 0-6 km BWD or EBWD 30-40 kt, 0-3 km SRH or ESRH > 100 m^2 s^{-2}, and MLLCL < 1500 m AGL (R. L. Thompson et al., 2003, 2012; Taszarek et al., 2020; Hanesiak et al., 2023). Based on the parameters shown in Table 1, local weather forecasters were concerned about tornadic supercells developing. However, a major uncertainty was whether the large cap (MLCIN < -50 J kg^{-1}) would be reduced enough for convection initiation. The combination of large CIN and high MLLCL (> 1500 m) also suggested that any developed supercell is likely going to be elevated (Coleman, 1990) and produce a strong outflow, both of which reduce tornado probability (E. N. Rasmussen & Blanchard, 1998; Davies, 2004; R. L. Thompson et al., 2012).

To project the mesoscale environment just before the Elie supercell initiation, we modified the 1800 UTC observed sounding using the 2100 UTC surface observations at Portage la Prairie, MB (WPG) and the Woodlands radar velocity azimuthal display (VAD)-

Table 1. Mesoscale storm parameters calculated using the observed, WRF, and ERA5 Winnipeg (XWI) soundings at 1800 UTC 22 June 2007. The 2100 UTC modified and WRF simulated sounding parameters at Portage la Prairie (WPG) are also shown.

	1800 UTC XWI obs.	1800 UTC XWI WRF	1800 UTC XWI ERA5	2100 UTC WPG mod.	2100 UTC WPG WRF
SBCAPE/SBCIN (J kg^{-1})	1010/-162	1641/-32	2004/-71	5581/0	4738/0
MLCAPE/MLCIN (J kg^{-1})	309/-226	1299/-73	713/-153	43/-286	3687/-2
MUCAPE/MUCIN (J kg^{-1})	2187/-71	1641/-32	2004/-71	5581/0	4738/0
$0-1$ km BWD (kt)	23	18	19	15	10
$0-6$ km BWD (kt)	39	33	36	30	43
EBWD (kt)	39	32	36	34	42
$0-3$ km SRH (m^2 s^{-2})	296	200	219	175	230
ESRH (m^2 s^{-2})	130	200	144	98	215
MLLCL (m AGL)	1595	1529	1434	1996	1319

derived winds (VAD data quality above 1.5 km ASL appears to worsen rapidly and thus was discarded and substituted with the 1800 UTC XWI sounding winds). The surface site and time were chosen since they were the closest to the Elie supercell initiation (see section 3.3.1) yet still free of convection contamination.

The modified sounding shows that the capping likely eroded away by late afternoon (Fig. 4b), with the SBCAPE and MUCAPE exceeding 5500 J kg^{-1} (Table 1). The 0-6 km BWD and EBWD (30-35 kt) and 0-3 km SRH and ESRH (100-200 m^2 s^{-2}) remained sufficient for tornadic supercells. However, because the modified sounding neglects the afternoon boundary-layer warming and moistening as well as the upper-level flow evolution, it only serves as a first guess of the local convective environment. Further analysis of the environment immediately before the Elie supercell initiation is provided in section 5.1 using the WRF simulation.

3.3 Storm initiation and the subsequent mesoscale evolution

In this subsection, we describe the radar and satellite observations during the late afternoon to early evening of 22 June 2007 with a focus on identifying the potential low-level trigger(s) of the Elie supercell. The broad storm evolution after the Elie supercell initiation is also briefly described. For a detailed description of the observed storm structure and evolution, readers are referred to Hobson (2011).

3.3.1 Storm initiation

At 2030 UTC 22 June 2007, a low-level mesoscale boundary (B1) was detected by radar to the southwest of Lake Manitoba (Figs. 5b, c). Its reflectivity and radial velocity shift signatures were faint at this time due to the radar beam altitude in relation to the depth of the low-level convergence (see the radar animation in the supplemental material). To the east of B1, lines of weak reflectivity, which we identified as horizontal convective rolls (HCRs; Weckwerth et al., 1997; Yang & Geerts, 2006), can be seen roughly aligned with the southwesterly surface flow across south-central Manitoba (only one is labeled as B2 for simplicity).

As B1 moved eastward, it became more apparent in the reflectivity and radial velocity scans (Figs. 5e, f). Deep cumulus convection began to develop along B1 (Fig. 5d). The Elie supercell (S1) was first detected on radar at 2200 UTC (Fig. 5e), rooted along B1 about 10 km to the northeast of WPG (Fig. 1). Two LBFs were identified along the southern shore of Lake Manitoba (labeled as B3 and B4). B3 brought an onshore (southwesterly to west-northwesterly) wind shift, a 1°C temperature drop, and a 3% relative humidity increase at Delta Marsh (Fig. 1) after it passed between 2100 UTC and 2200 UTC (not shown). A cold front approached the area from the north (see section 3.1) but it was not detected on radar well after S1 had initiated (B5 in Figs. 5h, k). Ahead of the cold front, the surface temperatures soared into low 30°Cs while the dew point reached low 20°Cs across southern Manitoba.

3.3.2 Storm evolution after initiation

After initiating, S1 intensified and moved eastward until it was located about 10 km north-northwest of Elie, with its anvil and precipitation shield blown to the southeast (Figs. 5g-i). S1 turned right relative to its original motion (east to south-southeast) between 2310 UTC and 2320 UTC while forming supercell structures, including a rotational couplet, hook echo, and wall cloud (Figs. 5k, l, 6a; Browning, 1977; Rotunno & Klemp, 1982; Weisman & Klemp, 1984; Klemp, 1987; Burgess & Lemon, 1990; Weisman & Rotunno, 2000; Davies-Jones, 2002; Markowski & Richardson, 2010). Two other prominent thunderstorms also had formed near S1 (S2 and S3; Fig. 5h). Between 2320 UTC and 2330 UTC, S1 produced a funnel cloud that reached the ground shortly after to form the Elie tornado (Figs. 6b, c). The tornado then struck Elie at 2350 UTC (Fig. 6d). At around the same time, S3 also matured into a supercell and produced an F3 tornado near Oakville, MB (Fig. 6e), while S2 weakened as a supercell without producing a tornado (not shown).

The radar analysis suggests that a low-level mesoscale boundary may be the primary triggering mechanism of the Elie supercell. However, the identity of this triggering boundary and the relative importance of the other boundaries (i.e., HCRs and LBFs) in storm initiation remain unclear. The real-case WRF simulation of this event was used to address two outstanding issues due to the lack of observations: 1) to better understand the local convective environment immediately before the Elie supercell initiation and 2) to identify and characterize the storm-triggering mechanism(s) of the Elie supercell. The simulation results follow.

4 Simulation overview and verification

We devote this section to the WRF simulation's performance in reproducing the Elie tornado event, focusing on the flow evolution leading up to the Elie supercell initiation. All PBL scheme sensitivity experiments exhibited similar synoptic- and mesoscale features (not shown), with the MYJ and QNSE scheme producing the strongest discrete supercells. The results from a simulation employing only D01-D03 with the MYJ and Eta schemes were found to be similar to those using all four domains, suggesting that 1 km grid-spacing was sufficient to resolve the processes contributing to the supercell initiation. For the ease of computation, the former was chosen for in-depth analysis.

4.1 Overview of the simulated flow

We begin by providing an overview of the simulated flow in southern Manitoba on 22 June 2007, focusing on the cloud and precipitation patterns during the late afternoon to early-evening periods. The simulated cloud top temperature was used to compare with

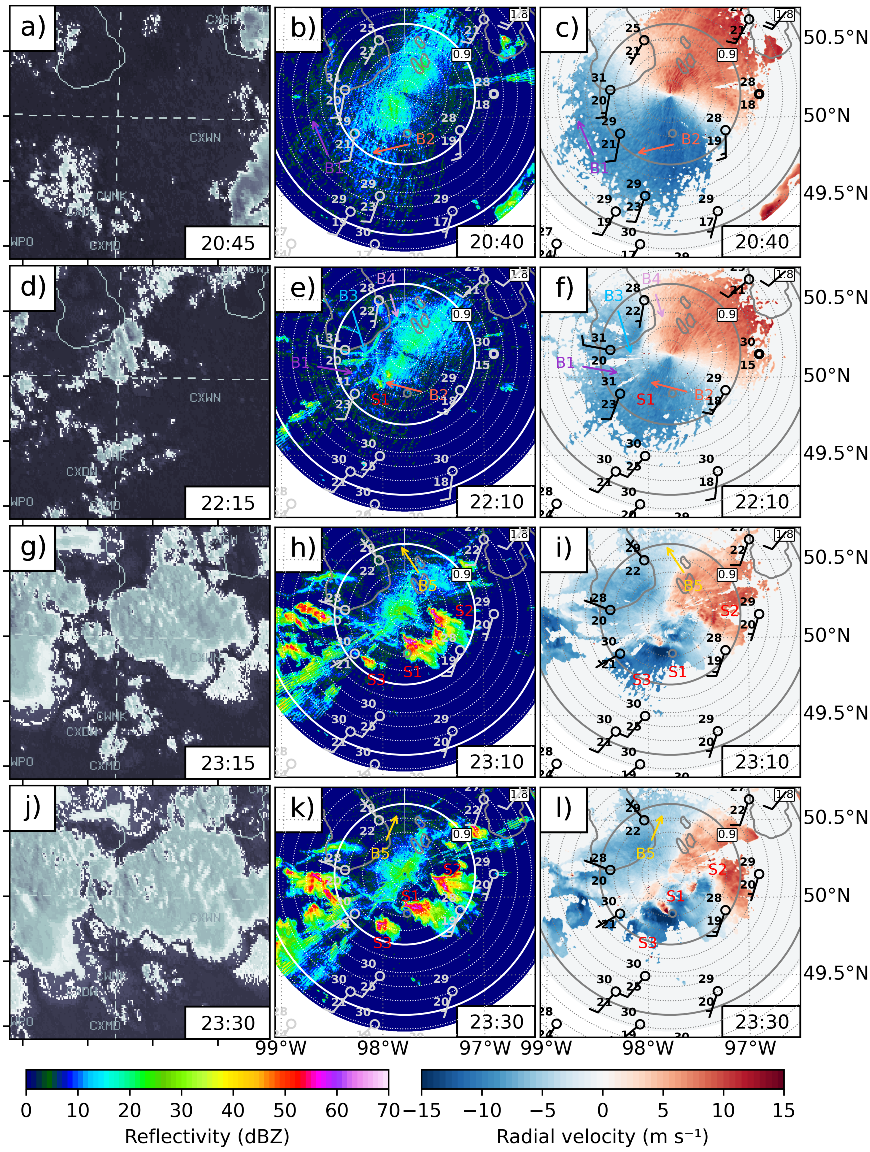

Figure 5. Observed visible satellite imagery (left column), radar reflectivity (center column), and radial velocity (right column) at the 0.5° elevation angle at a-c) 2040, d-f) 2210, g-i) 2310, and j-l) 2330 UTC 22 June 2007. Radar-detected mesoscale boundaries and supercells are annotated and labeled. Elie, MB is indicated by a gray circle. Station models in the area are also displayed. In the radar columns, the thick circles indicate the 50- and 100-km range rings, with the altitude (km ASL) at these ranges indicated in the boxes.

the visible satellite observations, while the simulated reflectivity at 1 km ASL was used to compare with the observed 0.5° reflectivity.

At 2040 UTC, a low-level convergence line with a few clouds was simulated to the southwest of Lake Manitoba (Fig. 7a, b), with the simulated 2-m air temperature and dew point around Elie reaching 28-31°C and 18-21°C, respectively, similar to observations (next section). Deep moist convection, including the precursor simulated Elie storm (SS1), began to initiate along the low-level convergence line at 2130 UTC, ∼ 40 min ear-

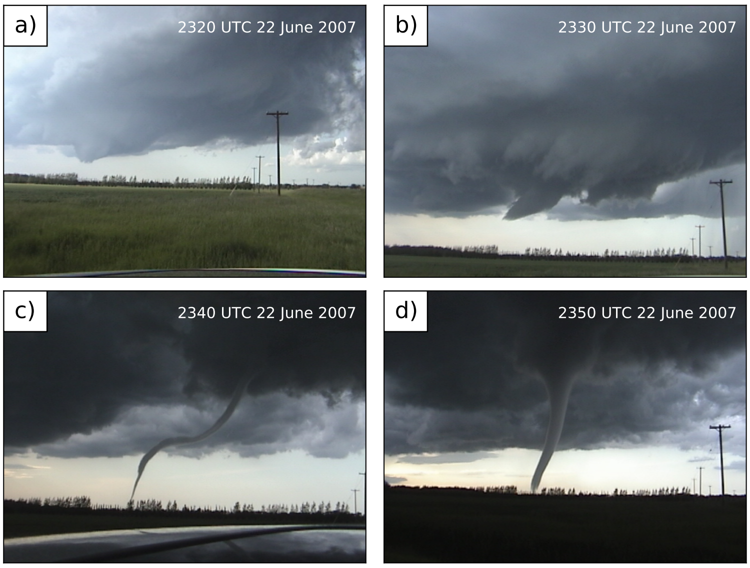

Figure 6. Photos of a) the Elie tornado's parent supercell, b) the Elie supercell with a funnel cloud, c) the Elie tornado touching down just north of Elie, d) and the Elie tornado in Elie. The camera shot times are indicated on the top right of each photo.

lier and $\sim$ 40 km farther west than that observed (Figs. 7c, d). The winds near Elie to the east of the convergence line were generally southwesterly with more westerly winds west of the line.

The simulated 2-5 km AGL updraft helicity (UH; Sobash et al., 2011; Naylor et al., 2012; Loken et al., 2017) was used to indicate mid-level mesocyclone presence in our simulation. After initiating, SS1 propagated eastward and developed an UH core on its western flank by 2230 UTC, with its anvil sheared to the southeast (Figs. 7e, f). As with the observed storm, the accumulated 10-min maximum UH track (since 2000 UTC 22 June 2007) suggests that SS1 traveled eastward and then southeastward(crossref Figs. 7 and 5); reaching Elie at around 2300 UTC, $\sim$ 50 min earlier than the observed (Fig. 7g, h). Some vigorous cells were also simulated to the north and south of SS1. A few of these cells briefly exhibited mid-level rotation, agreeing with the observed convection distribution where multiple supercells existed simultaneously around the Elie cell.

4.2 Simulated surface conditions

The simulation root-mean-squared error (RMSE), bias, and index of agreement (IOA) for surface air temperature (T_{2m}), dew point (Td_{2m}), wind speed (V_{10m}), and wind direction ($\angle V_{10m}$) were computed using the hourly observed and simulated values at all surface stations described in section 2.1.5 and presented in Table 2. The differences between the observed and forecast $\angle V_{10m}$ were adjusted using the method described in (Lascaux et al., 2013) to account for angular measurements. Wind measurements at non-standard meteorological stations (i.e., Morris and Selkirk, MB) were excluded to avoid possible data quality issues. The evaluation period was between 1200 UTC to 2100 UTC 22 June 2007 to focus on the pre-Elie storm period.

Based on the values in Table 2, WRF appeared to reasonably capture the observed surface conditions during the period examined, with the variables' RMSE and bias generally small and IOA > 0.70. The largest errors exist in Td_{2m} and V_{10m} likely due to

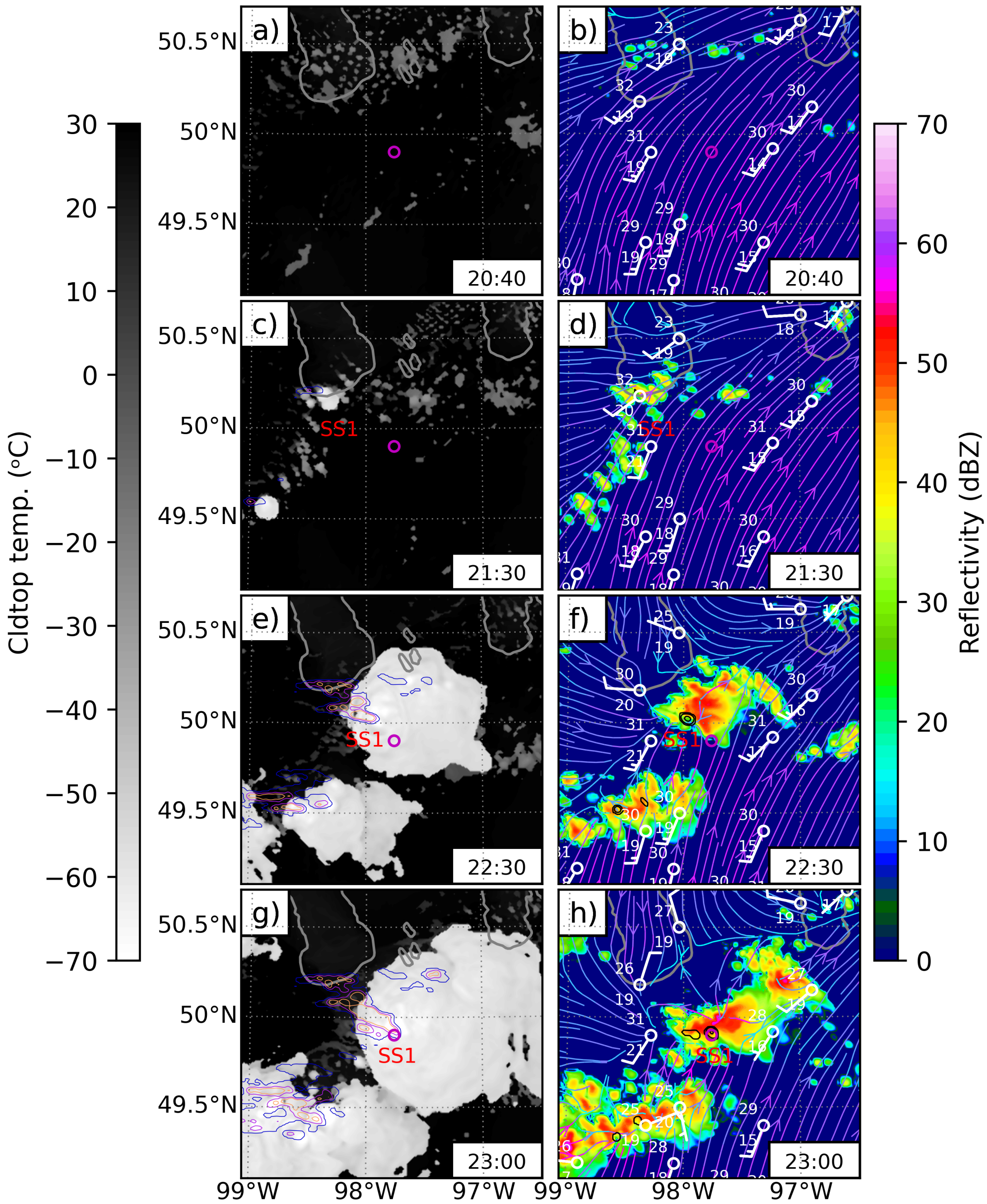

Figure 7. Left: The WRF simulated cloud top temperature (filled) and accumulated 10-min maximum 2-5 km AGL updraft helicity (solid; in contours of 100, 300, 500 and 700 m^2 s^{-2}). Right: The WRF simulated 1 km ASL reflectivity (filled), 2-5 km AGL updraft helicity (black solid; in contours of 75, 150, 300, and 500 m^2 s^{-2}), 10-m streamlines, and the simulated conditions on the hour at the surface stations in the area (see Fig. 1). Elie is indicated by a magenta circle. The plotted times (UTC) are indicated on the lower right of each panel.

their highly locally varying nature, which was exacerbated by the lack of observations. The model's misrepresentation of the observed early-day precipitation likely partly contributed to the remaining errors. Immediately before the observed Elie supercell initiation, the WRF simulated T_{2m}, Td_{2m}, V_{10m}, and $\angle V_{10m}$ appear to agree well with the observations near the storm initiation region (not shown).

Table 2. Simulation RMSE, bias, and IOA for T_{2m}, Td_{2m}, V_{10m}, and $\angle V_{10m}$ evaluated between 1200 UTC and 2100 UTC 22 June 2007.

	T_{2m}	Td_{2m}	V_{10m}	$\angle V_{10m}$
RMSE	1.9	2.4	1.9	46.1
Bias	0.3	-1.3	0.4	5.8
IOA	0.96	0.80	0.70	0.80

4.3 Winnipeg sounding and the large-scale pattern

The 1800 UTC WRF simulated sounding at the nearest model grid point to the Winnipeg radiosonde launch site was used to compare against the observed sounding (Fig. 4a). The simulated 1800 UTC CAPE (CIN) at Winnipeg were generally 600-1000 (50-150) J kg^{-1} larger (smaller) than the observed, except for MUCAPE (Table 1). These discrepancies may be partly owing to a 2-3°C simulation warm bias below 900 hPa and mesoscale ascent ahead of the simulated early-afternoon convection near Winnipeg temporarily weakening the low-level cap (not shown). After the simulated convection exited the area by 1830 UTC, the cap quickly rebuilt over Winnipeg before eroding away (not shown).

The simulated BWD and SRH at XWI at 1800 UTC 22 June 2007 were overall weaker than the observed (except for ESRH), especially for the simulated 0-3 km SRH ($\sim$ 30% too weak). The error may be partly due to the simulated wind direction being more westerly than the observed from the surface up to 800 hPa (hence less veering; Fig. 4a). In their studies of European and Canadian tornadic storm environments, Taszarek et al. (2021) and Hanesiak et al. (2023) found that ERA5 reasonably captured the observed vertical atmospheric profiles and the derived convective parameters in these regions. For the Elie event, the 1800 UTC WRF-derived BWD and SRH at XWI were comparable to those calculated from the ERA5 sounding (Table 1). The temperature advection, pressure (or geopotential height), and convective parameter patterns over the Canadian Prairies were also broadly similar between WRF and ERA5 throughout the day (not shown). Thus, WRF appeared to adequately reproduce the event's large-scale flow.

5 Immediate storm environment and storm-triggering mechanisms

5.1 Immediate storm environment

To evaluate the local storm environment just before the simulated Elie supercell initiation at 2130 UTC 22 June 2007, we examined the 2100 UTC 22 June 2007 simulated convective parameters near the storm initiation site at WPG. For the sounding analysis, the data from D03 was used, while the data from D01 was used for the map analysis unless noted otherwise. To demonstrate the significance of the simulated environmental parameters in terms of the tornadic supercell environments, we also computed the supercell composite parameter (SCP) and significant tornado parameter (STP):

$$SCP = \frac{MUCAPE}{1000\ J\ kg^{-1}} \frac{EBWD}{20\ m\ s^{-1}} \frac{ESRH}{50\ m^2\ s^{-2}} \quad (1)$$

$$STP = \frac{MLCAPE}{1500\ J\ kg^{-1}} \frac{EBWD}{20\ m\ s^{-1}} \frac{ESRH}{150\ m^2\ s^{-2}} \frac{2000\ m - MLLCL}{1000\ m} \frac{MLCIN + 200\ J\ kg^{-1}}{150\ J\ kg^{-1}} \quad (2)$$

, where all terms have been previously defined. Readers shall refer to R. L. Thompson et al. (2004c) and R. L. Thompson et al. (2012) for the conditions that apply to the right-hand-side terms of both equations.

5.1.1 The 2100 UTC simulated WPG sounding

The SCP and STP computed based on the 2100 UTC simulated sounding (Figs. 4b and Table 1) were 20 and 2.6, respectively. Compared to other tornado events in the U.S., the former was well above the 25th-75th percentile range (the interquartile range, hereafter) for discrete, right-moving tornadic (RMdT) supercell cases, while the latter fell within the interquartile range (i.e., the typical range) for significantly tornadic (EF2+) RMdT (sigtor) supercells (Fig. 8; R. L. Thompson et al., 2012). The large SCP and STP were mainly a result of the large MUCAPE and MLCAPE as they both exceeded the typical values found in the RMdT and sigtor supercell cases in the U.S. (> 3500 J kg^{-1}), while EBWD and ESRH both fell towards the lower end of the distributions (< 45 kt), especially for sigtor supercells (Fig. 8). The Elie event also featured a higher MLLCL (> 1300 m AGL) than the majority of sigtor supercell events in the U.S. (Fig. 8b). Similar trends were found when comparing the 2100 UTC simulated SCP and STP and their constituent parameters to those derived based on the Canadian sigtor events (see Hanesiak et al. (2023)). However, if comparing only against the summertime sigtor supercell cases in the U.S., the 2100 UTC simulated EBWD, ESRH, and MLLCL at WPG were rather typical for these events (Fig. 8b; R. L. Thompson et al., 2012). The middle-to-high-end simulated SCP and STP compared to those typically found in other significant tornado events in North America suggests that the late-afternoon environment near Elie posed a substantial threat of sigtor supercells.

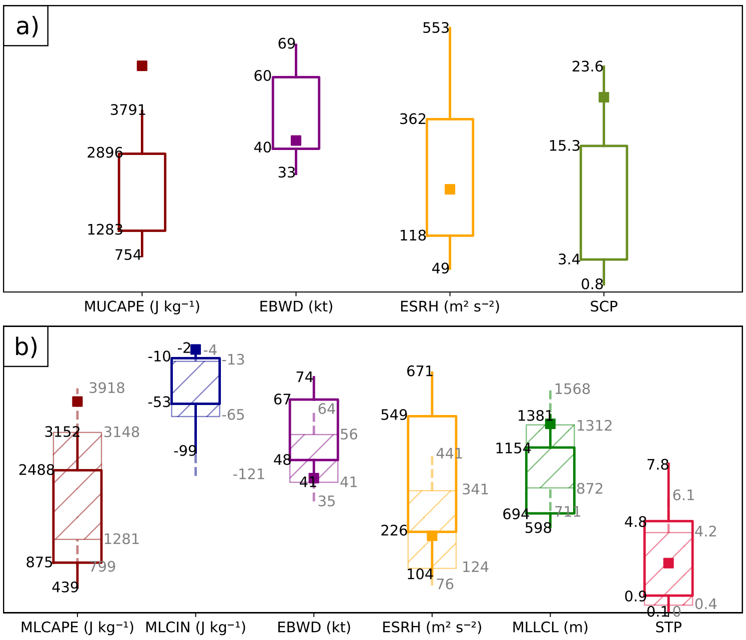

Figure 8. Box-whiskers (the boxes denote the 25th-75th percentiles; the whisker tips denote the 10th-90th percentiles) of a) SCP and its component parameters for RMdT (discrete, right-moving tornadic) supercells in the U.S. and b) STP and its component parameters for U.S. sigtor (significantly tornadic) supercell events. In b), the hollow boxes with solid whiskers denote the distribution derived based on all-year events regardless of the season and the hatched boxes with dashed whiskers represent those derived based on summertime events only. The 2100 UTC WRF simulated values (texts omitted) at WPG are marked by filled squares. Adapted from R. L. Thompson et al. (2012).

5.1.2 The 2100 UTC simulated convective parameter spatial patterns

Figure 9 shows that low-level moisture and wind shear were enhanced over a narrow band stretching from the Manitoba-North Dakota border, over WPG, and into southern Lake Manitoba, hence the locally larger CAPE, lower LCL, and greater EBWD and ESRH. This feature was likely induced by an outflow boundary associated with the simulated convection that moved across southern Manitoba between 1600 UTC and 1800 UTC. Outflow boundaries can locally enhance moisture and/or shear, thereby increasing the likelihood of tornadic supercells (e.g., Maddox et al., 1980). The simulated SCP and STP were indeed enhanced within the band of large conditional instability and shear near WPG relative to the west-east adjacent areas (Fig. 9f).

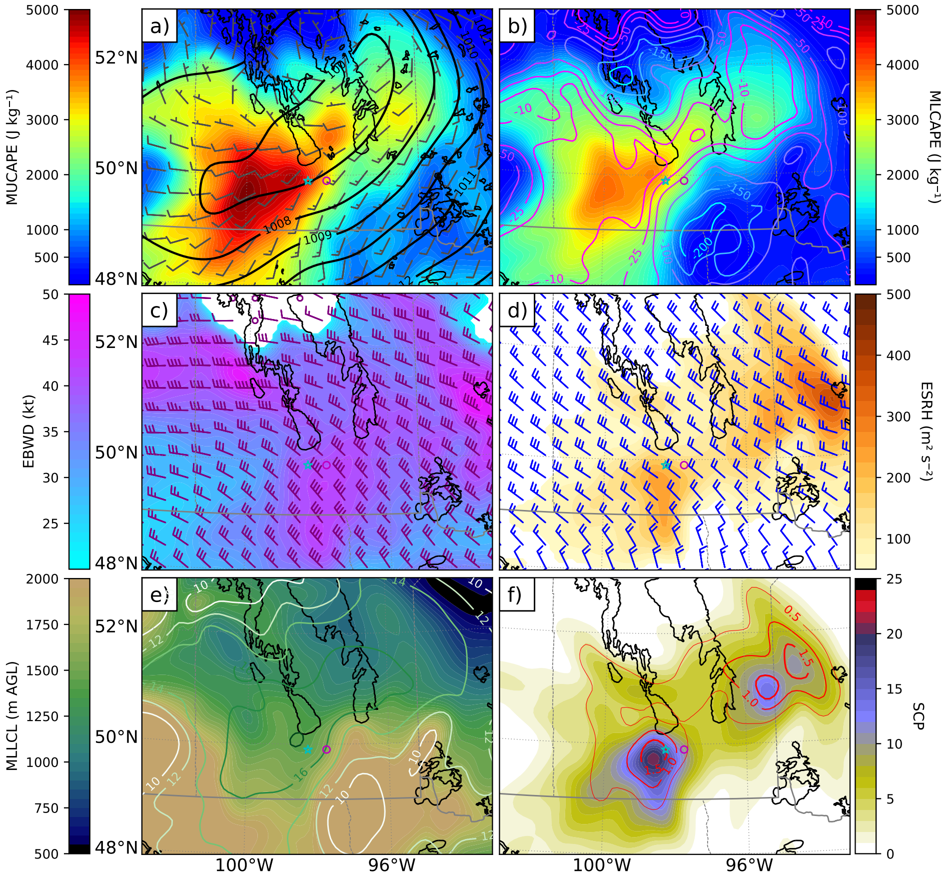

Figure 9. Maps of the WRF simulated a) MUCAPE (filled), sea level pressure (solid), and 10-m wind barbs, b) MLCAPE (filled), MLCIN (solid), c) EBWD speed (filled) and barbs, d) ESRH (filled) and Bunkers storm motion barbs, e) MLLCL (filled) and the lowest 100-mb averaged dew point (solid; in °C), and f) SCP (filled) and STP (solid) at 2100 UTC 22 June 2007. Elie is indicated by a circle, while WPG is indicated by a star.

A cluster of convection was observed propagating across southern Manitoba between 1800 UTC to 2000 UTC 22 June 2007. Here, we investigate whether this convection also locally enhanced the immediate tornado environment near Elie. At 2000 UTC, an area of reduced reflectivity (suppressed HCRs) denoting the cold pool produced by this convection was detected (Figs. 10a, b). The gridded surface wet-bulb potential temperature (θ_w) calculated using the surface observations shows that the cold pool may have tightened and orientated the surface θ_w contours latitudinally between WPG and Elie, thereby influencing the local pressure gradient and wind patterns. The radar VAD shows that the low-level winds turned southwesterly within the storm's outflow (Fig. 10a), shifted back to south-southwesterly as the cold pool moved east out of the area, and remained so until storm initiation (Figs. 10b, c).

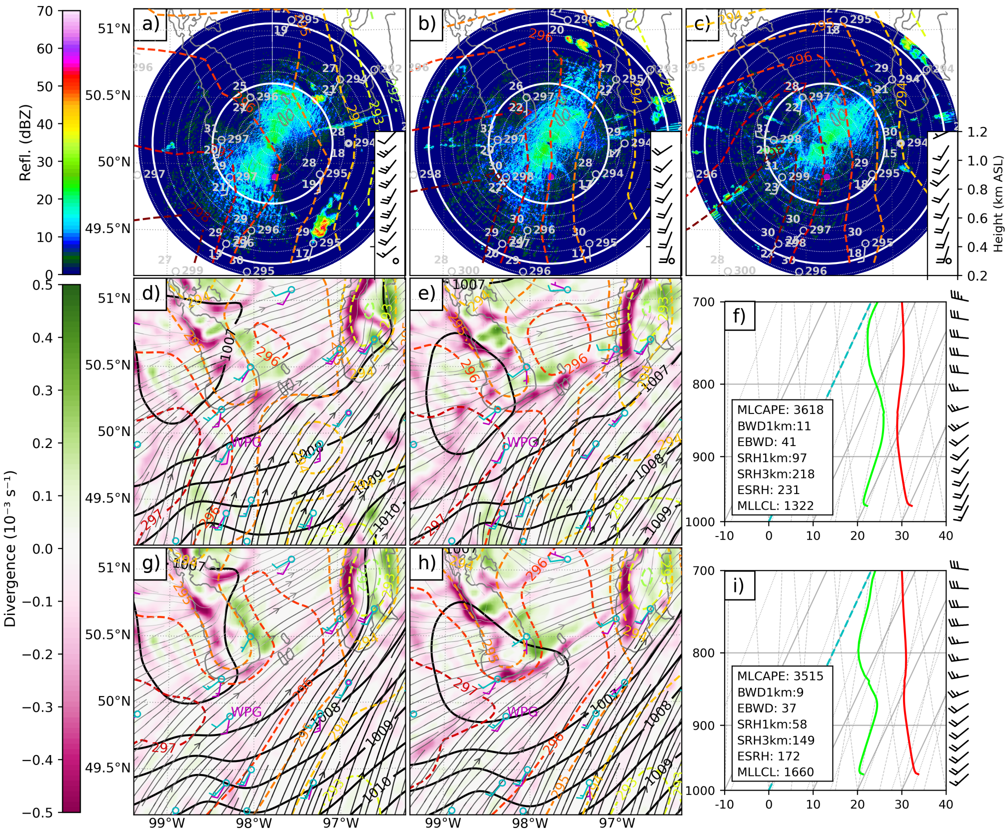

Figure 10. Observed radar reflectivity (filled), surface θ_w (dashed), and station models (temperature: top left, dew point: bottom left, and θ_w: center right) at a) 2000 UTC, b) 2100 UTC, and c) 2200 UTC 22 June 2007. The Woodlands, MB radar VAD-derived wind profiles at these times are also shown at the bottom right of these panels. d, e) Simulated 10-m divergence (filled), surface θ_w (dashed), SLP (black solid), 10-m streamlines, and the observed (purple) and simulated (cyan) surface station wind barbs at 2000 UTC and 2100 UTC, respectively, from the MP simulation. g, h) Same as in d, e), but from the NOMP simulation. f) Simulated WPG sounding and selected convective parameters from the MP simulation at 2100 UTC 22 June 2007. i) Same as in f), but from the NOMP simulation.

To isolate the outflow's effects on the local storm environment, we performed another WRF simulation with the microphysics turned off (NOMP). D02 data was used for this analysis. The original simulation (MP) produced similarly orientated surface θ_w contours behind the simulated afternoon convection (Figs. 10d, e), while the NOMP simulation showed less latitudinally-oriented and farther east-located tight θ_w contours (Figs. 10g, h). Perhaps as a result, the 2100 UTC simulated winds between the surface and 800 hPa at WPG were more southerly in the MP simulation than those in the NOMP simulation, better agreeing with the observations (Figs. 10e, h; crossref Figs. 10f, i with Figs. 10b, c). The greater low-level veering likely resulted in larger simulated BWD and SRH near WPG in the MP simulation vs. the NOMP simulation (Figs. 10f, i).

Both the MP and NOMP simulations produced a mesoscale boundary that later triggered the Elie storm in the former. The more southerly flow in the MP simulation more strongly interacted with the boundary, thereby producing greater low-level convergence (hence moisture convergence; not shown), larger MLCAPE, and lower MLLCL near WPG than in the NOMP simulation (Figs. 10e, h, f, i). Overall, the observed remnant outflow boundary likely enhanced the immediate storm environment near Elie and the simulation appeared to capture this effect.

5.2 Triggering mechanism

In this section, we investigate the potential triggering mechanism(s) of the Elie supercell using the simulated low-level flow in the afternoon of 22 June 2023 leading up to the simulated convection initiation time. Two averaged cross sections (along their short axes) each composed of 40 individual transects spaced $\sim$ 1 km apart were created to diagnose the vertical structure of the simulated low-level flow (see Fig. 12 for locations).

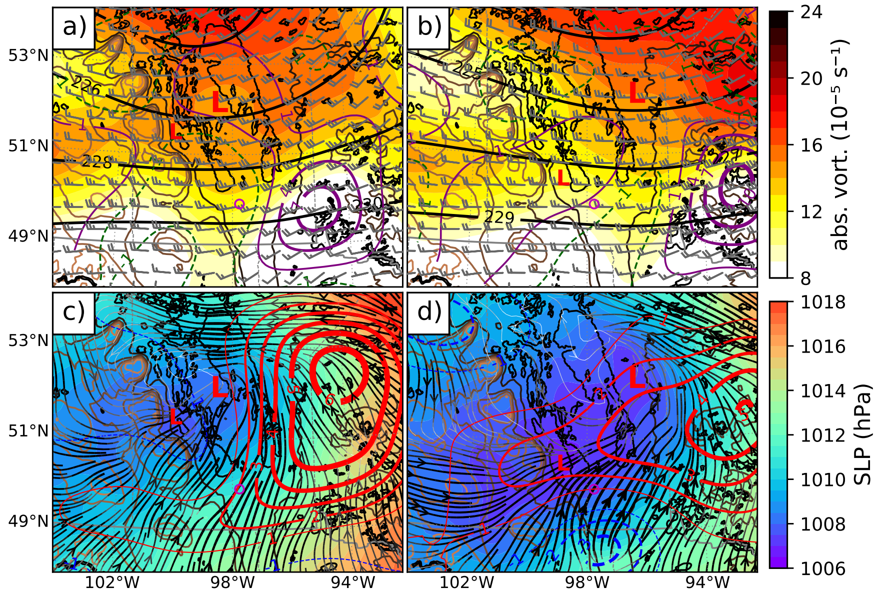

Figure 11. Top panels: averaged 850-700 hPa simulated absolute vorticity (filled), geopotential height (black solid; in decameters), wind barbs, and 850-700 hPa differential absolute vorticity advection (purple solid for cyclonic, green for anticyclonic; in 10^{-9} s^{-2}) at a) 1600 UTC and b) 2000 UTC 22 June 2007. Bottom panels: simulated SLP (filled), averaged 850-700 hPa vertical velocity (red for ascent, blue for descent; in cm s^{-1}), and 10-m streamlines at c) 1600 UTC and d) 2000 UTC 22 June 2007. The synoptic low pressure system is labeled with a big 'L', while the lee low is marked with a small 'L'.

At 1600 UTC, a mesoscale low developed downwind (to the east) of Duck Mountain (Fig. 1). We suspect that this low may have been a lee low (Palmén & Newton, 1969; McGinley, 1982; Steenburgh & Mass, 1994; Holton, 2004) that formed within the synoptic low as low-level cyclonic flow over eastern Saskatchewan moved east and descended into the lower-laying RRV (Figs. 2, 11a). As in ERA5, 850-700 hPa cyclonic differential vorticity advection and the associated mid-level ascent occurred above the mesoscale low in the late afternoon (Figs. 3d, 11b), promoting further deepening of the low as it propagated southeastward along the western slope of RRV (Figs. 1, 11d).

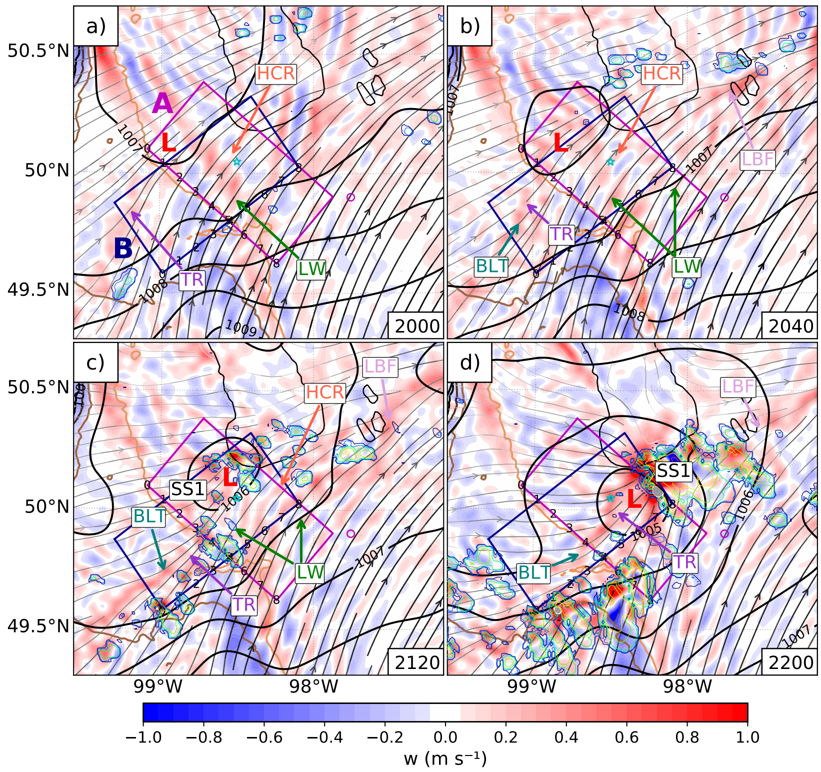

Figure 12. Simulated vertical motion at 1 km AGL (filled), 1-km ASL reflectivity (rainbow contours), SLP (black contours), and 10-m streamlines. The simulated boundaries (TR=surface trough, HCR=horizontal convective rolls, BLT=boundary layer thermals, LBF=lake breeze front, LW=lee waves) and Elie supercell (SS1) are also labeled. The locations of the averaged cross sections (A and B) are indicated by the boxes. 'L' indicates the approximate location of the mesoscale low pressure center. The times shown are a) 2000 UTC, b) 2040 UTC, c) 2120 UTC, and d) 2200 UTC 22 June 2007.

A trough (TR in Fig. 12) developed to the southwest of the low near 2000 UTC, with CBL thermals (BLTs) propagating northeastward along it. Beginning at 2040 UTC, a few shallow cumuli formed where the TR-BLT forcing interacted above the moisture pool between the TR and the remnant outflow (see section 5.1.2; Figs. 12b, c, and 13c-f). One of the simulated cells underwent rapid growth after coinciding with a simulated lee-wave crest and matured into the simulated Elie supercell (SS1 in Fig. 12). Lee waves were not observed over southern Manitoba around storm initiation time, possibly because they were weak, resided above the lowest radar scan, and peaked above the CBL top where backscatters were scarce (1.5-2 km vs. 1 km ASL; crossref Figs. 13, 5). HCRs and the Lake Manitoba lake breeze front (LBF) were also simulated around this time (Figs. 12 and 13). Based on the simulation results, lee waves likely invigorated the convection instead of triggered it on this day, similarly for the HCRs. The Lake Manitoba LBFs and the cold front did not appear to contribute directly to the Elie storm initiation, as both the observation and simulation suggest that the storm's initial updrafts originated elsewhere. After initiation, SS1 propagated eastward towards Elie (Fig. 12d)

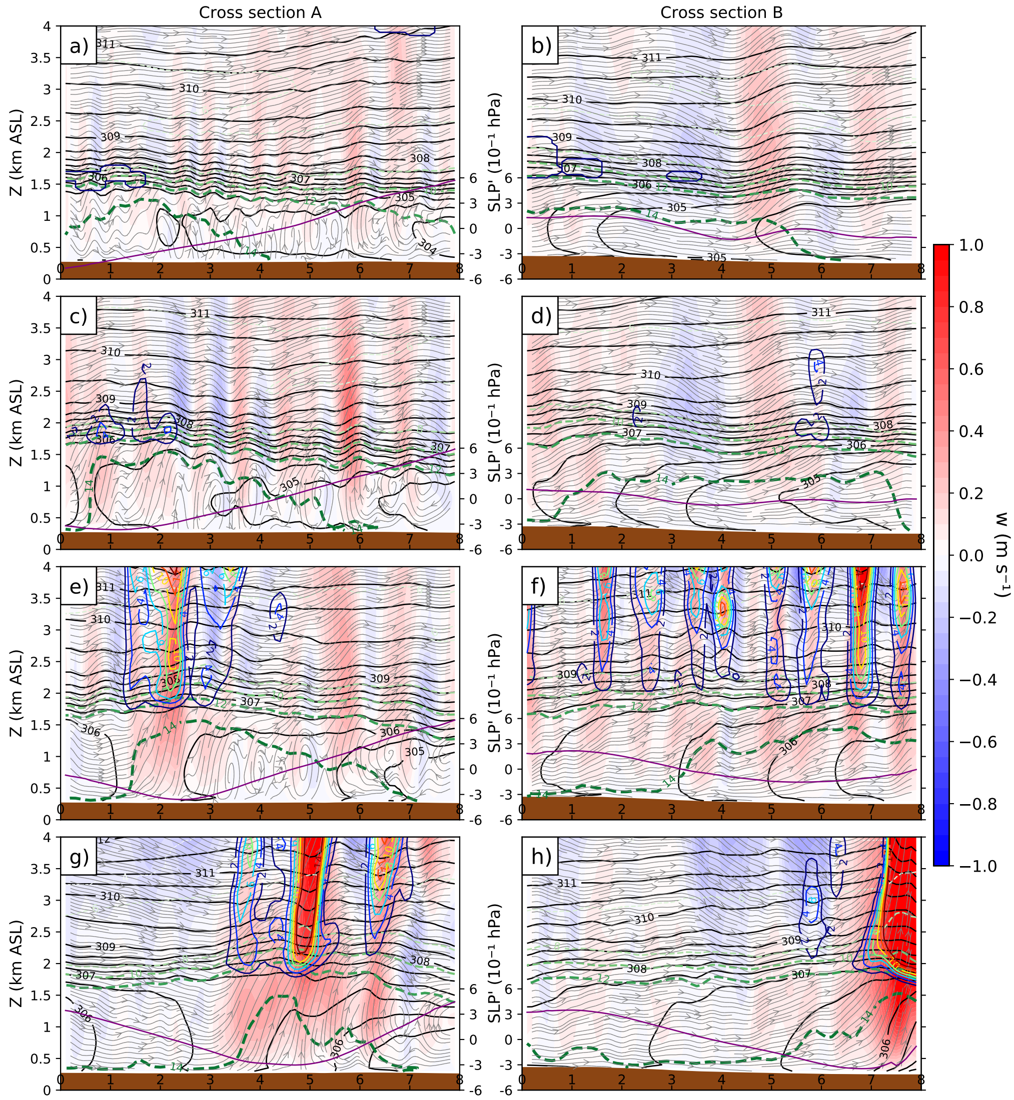

Figure 13. Averaged simulated cross sections (see Fig. 12 for their locations) of vertical motion (filled), cloud and ice water mixing ratio (rainbow contours; 10^{-2} g kg^{-1}), potential temperature (black contours), water vapor mixing ratio (dashed contours; g kg^{-1}), and streamlines. The SLP perturbation relative to the cross-section mean is also plotted as purple lines. The times shown are a-b) 2000 UTC, c-d) 2040 UTC, e-f) 2120 UTC, and g-h) 2200 UTC 22 June 2007.

6 Conclusions

To identify and characterize the synoptic scale and mesoscale features that contributed to the formation of the 22 June 2007 Elie, Manitoba F5/EF5 tornado (the first and only F5/EF5 tornado in Canada to this date), a comprehensive meteorological analysis was undertaken using available observations and a high-resolution, cloud-resolving, real-case WRF simulation of this event. This study complements Hobson (2011) observational analysis of this event by better characterizing the storm environment immediately before the storm initiation and the storm-triggering mechanism(s). The main results are summarized below:

1. The Elie supercell formed under a quiescent upper-level regime with little upper-level forcing for ascent, suggesting the importance of lower-troposphere large-scale and mesoscale forcing in priming the convective environment.
2. The convective environment near Elie immediately before storm initiation was favorable for the development of tornadic supercells, highlighted by the very large conditional instability (convective available potential energy > 4000 J kg^{-1}) and moderate deep-layer shear (effective wind shear $\sim$ 40 kt; effective storm-relative helicity > 200 m^2 s^{-2}). However, an important result is that both ingredients were enhanced by a remnant cold pool left behind by early afternoon convection and the storm-triggering boundary itself.
3. Despite the local enhancement, the shear parameters were not particularly impressive compared to those typically found in the significantly tornadic supercell cases in the United States considering all seasons, but rather typical compared to just the summertime cases (R. L. Thompson et al., 2012).
4. The primary triggering mechanism of the Elie supercell was the interaction between boundary-layer thermals and a surface trough associated with a mesoscale low pressure system that developed over the western slope of the Red River Valley. The western Manitoba terrain (lee troughing effect) and 850-700 hPa cyclonic differential vorticity advection may both have played roles in the formation and/or intensification of the low.
5. Other mesoscale features such as lee waves and horizontal convective rolls may have provided additional lifting that invigorated convection, including the Elie supercell.

Terrain lee effects have been observed and studied near many major mountains around the world, including the Alps (e.g., Speranza, 1975; Buzzi & Tibaldi, 1978; McGinley, 1982), the Canadian and U.S. Rockies (e.g., Chung et al., 1976; Steenburgh & Mass, 1994), the Tibetan Plateau in China (e.g., Chung et al., 1976; Q. Li et al., 2016), and the Andes (e.g., Chung et al., 1977; K. L. Rasmussen & Houze Jr., 2016). They also have been documented to the lee of shallower mountains such as the Appalachians (e.g., D. B. Thompson, 2012). To the authors' knowledge, orographic lee phenomena induced by the even shallower Manitoba terrain have not received any attention. Contrary to the common notion that Manitoba terrain have minimal influences on the regional convection pattern (e.g., Erfani, 1999), this study suggests that terrain-induced features may indeed have effects in Manitoba. More numerical experiments by varying the regional topography and land cover are required to better understand the topography's impacts on convection initiation during the Elie event. Like the climatology study by Kovacs and Kirshbaum (2016) near Montréal, Québec, more meteorological observations and numerical experiments may be needed to diagnose the effects of Manitoba orography on the regional convection pattern.

Open Research Section

Data availability statement

The complete ERA5 data (Hersbach et al., 2017) is publicly available at the Copernicus Climate Change Service (C3S) Data Store (CDS) at `https://cds.climate.copernicus.eu/cdsapp#!/dataset/reanalysis-era5-complete?tab=overview`. The radar and sounding observations are publicly available upon request from ECCC. The surface observations are publicly available for download from the ECCC Historical Climate Archive at `https://climate.weather.gc.ca/historical_data/search_historic_data_e.html`. The GFS analysis used for WRF initialization can be download from the National Center for Environmental Information (NCEI) data server at `https://www.ncei.noaa.gov/products/weather-climate-models/global-forecast`. The GHRSST dataset can be viewed on National Aeronautics and Space Administration's Worldview data viewer at `https://worldview.earthdata.nasa.gov/` by searching for the GHRSST dataset in the data layer tab (under sea surface temperature) and select the correct date. The WRF output and processed data used in this paper can be accessed at `https://doi.org/10.5281/zenodo.10125834`.

Software availability statement

The WRF model and its preprocessing system (WRF Preprocessing System; WPS) used in this study can be downloaded from `https://github.com/wrf-model/WRF/releases?page=2` and `https://github.com/wrf-model/WPS/releases`. The calculations and figures in this paper were performed/produced using Python v3.8.5 (Python Software Foundation, 2020). The WRF output was analyzed using WRF-Python v1.3.2 (Ladwig, 2017), licensed under the Apache License v2.0. Many of the thermodynamic and kinematic calculations (excluding the convective parameters) and Skew-T plots were made using MetPy v0.12 (May et al., 2020), licensed under the BSD 3 Clause license. The radar observations were analyzed using ARM-PyART v1.11.3 (Helmus & Collis, 2016), licensed under the BSD 3 Clause license. The convective parameters were computed using SHARPpy v1.4.0 (Blumberg et al., 2017), licensed by the SHARPpy license at `https://sharppy.github.io/SHARPpy/license.html`. All figures were made using Matplotlib v3.2.2 (Hunter, 2007; Caswell et al., 2020), available under the Matplotlib license at `https://matplotlib.org/`. Map plots were made using Basemap v1.2.2 (Whitaker, 2020), available under the Basemap license at `https://github.com/matplotlib/basemap`.

Acknowledgments

This research was kindly funded by a Natural Sciences and Engineering Research Council (NSERC) Discovery Grant and the Northern Tornadoes Project. The fourth author received funding from the Polish National Science Center (grant no. 2020/39/D/ST10/00768). The WRF numerical simulations were performed and stored on the Cedar supercomputer, under the auspice of Digital Research Alliance of Canada. Special thanks to Daniel Michaelson and Jason Knight for sharing the radar observations.

References

Alexander, L. S., Sills, D. M. L., & Taylor, P. A. (2018). Initiation of convective storms at low-level mesoscale boundaries in southwestern Ontario. *Wea. Forecasting*, *33*, 583-598. doi: https://doi.org/10.1175/WAF-D-17-0086.1

Balaji, V., & Clark, T. L. (1998). Scale selection in locally forced convective fields and the initiation of deep cumulus. *J. Atmos. Sci.*, *45*, 3188-3211.

Balsamo, G., Dutra, E., Albergel, C., Munier, S., Calvet, J. C., Munoz-Sabater, J., & de Rosnay, P. (2018). ERA-5 and ERAInterim driven ISBA land surface model simulations: Which one performs better? *Hydrol. Earth Syst. Sci.*, *22*, 3515–3532.

Bisson, M. J. R., & Paola, R. (2000). *Brunkild tornado event 24 July 2000: An example of tornadogenesis in a low shear multicell storm environment over southern Manitoba, Canada.* Retrieved 2023-07-18, from `https://www.umanitoba.ca/environment/envirogeog/weather/radarstudies/brunkild/BrunkildTornado.html`

Blumberg, W. G., Halbert, K. T., Supinie, T. A., Marsh, P. T., Thompson, R. L., & Hart, J. A. (2017). SHARPpy: An open-source sounding analysis toolkit for the atmospheric sciences. *Bull. Amer. Meteor. Soc.*, *98*(8), 1625-1636. Retrieved from `https://github.com/sharppy/SHARPpy` doi: https://doi.org/10.1175/BAMS-D-15-00309.1

Brooks, H. E. (2004). On the relationship of tornado path length and width to intensity. *Wea. Forecasting*, *2*, 310-319. doi: https://doi.org/10.1175/1520

-0434(2004)019⟨0310:OTROTP⟩2.0.CO;2
Brooks, H. E., Doswell III, C. A., & Cooper, J. (1994). On the enviornments of tornado and nontornadic mesocyclones. *Wea. Forecasting*, *9*, 606-618. doi: https://doi.org/10.1175/1520-0434(1994)009⟨0606:OTEOTA⟩2.0.CO;2.41
Brooks, H. E., Lee, J. W., & Craven, J. P. (2003). The spatial distribution of severe thunderstorm and tornado environments from global reanalysis data. *Atmos. Res.*, *67-68*, 73-94. doi: https://doi.org/10.1016/S0169-8095(03)00045-0
Browning, K. A. (1977). The structure and mechanism of hailstorms. *J. Atmos. Sci.*, *21*, 634-639.
Bryan, G. H., Wyngaard, J. C., & Fritsch, J. M. (2003). Resolution requirements for the simulation of deep moist convection. *Mon. Wea. Rev.*, *131*, 2394-2416.
Bullas, J. M., & Wallace, A. F. (1988). The Edmonton tornado, July 31, 1987 [Preprints,]. In *Preprints, 15th conference on severe local storms* (p. 437-443). Baltimore, MD.
Bunkers, M. J., Barber, D. A., Thompson, R. L., Edwards, R., & Garner, J. (2014). Choosing a universal mean wind for supercell motion prediction. *J. Operational Meteor.*, *2*, 115-129.
Burgess, D. W., & Lemon, L. R. (1990). Severe Thunderstorm Detection by Radar. In D. Atlas (Ed.), *Radar in meteorology: Battan memorial and 40th anniversary radar meteorology conference* (p. 619-647). Boston, MA: American Meteorological Society.
Buzzi, A., & Tibaldi, S. (1978). Cyclogenesis in the lee of the Alps: a case study. *Quart. J. Roy. Meteor. Soc.*, *104*, 271-287.
Caswell, T. A., Droettboom, M., Lee, A., Hunter, J., Firing, E., Stansby, D., ... Katins, J. (2020). *matplotlib/matplotlib: Rel: v3.2.2.* doi: 10.5281/zenodo.3898017
Charlton, R., Kachman, B., & Wojtiw, L. (1995). Urban hailstorms - A view from Alberta. *Nat. Hazards*, *12*, 29-75.
Chiba, O. (1993). The turbulent characteristics in the lowest part of the sea breeze front in the atmospheric surface layer. *Bound.-Layer Meteor.*, *65*, 181-195.
Chung, Y.-S., Hage, K. D., & Reinelt, E. R. (1976). On lee cyclogenesis and airflow in the Canadian Rocky Mountains and the east Asian mountains. *Mon. Wea. Rev.*, *104*, 879-891.
Chung, Y.-S., Hage, K. D., & Reinelt, E. R. (1977). On the orographic influence and lee cyclogenesis in the Andes, the Rockies, and the east Asian mountains. *Arch. Met. Geoph. Biokl., Ser.*, *26*, 1-12.
Coffer, B. E., Taszarek, M., & Parker, M. D. (2020). Near-ground wind profiles of tornadic and nontornadic environments in the United States and Europe from ERA5 reanalyses. *Wea. Forecasting*, *35*, 2621-2638.
Coleman, B. R. (1990). Thunderstorms above frontal surfaces in environments without positive CAPE. Part I: A climatology. *Mon. Wea. Rev.*, *118*, 1103-1121. doi: https://doi.org/10.1175/1520-0493(1990)118⟨1103:TAFSIE⟩2.0.CO;2
Crosman, E. T., & Horel, J. D. (2012). Idealized large-eddy simulations of sea and lake breezes: Sensitivity to lake diameter, heat flux and stability. *Bound.-Layer Meteor.*, *144*, 309-328. doi: https://doi.org/10.1007/s10546-012-9721-x
Curry, M. (2015). *An examination of lake breezes in southern Manitoba* (Unpublished master's thesis). University of Manitoba, Winnipeg, MB. (125 pp)
Curry, M., Hanesiak, J., Kehler, S., Sills, D. M. L., & Taylor, N. M. (2016). Ground-based observations of the thermodynamic and kinematic properties of lake-breeze fronts in southern Manitoba, Canada. *Bound.-Layer Meteor.*, *163*, 143-159. doi: https://doi.org/10.1007/s10546-016-0214-1
Dailey, P. S., & Fovell, R. G. (1999). Numerical simulation of the interaction between the sea-breeze front and horizontal convective rolls. Part I: Offshore ambient flow. *Mon. Wea. Rev.*, *127*, 858-878.
Davies, J. M. (2004). Estimations of CIN and LFC associated with tornadic and

nontornadic supercells. *Wea. Forecasting*, *19*, 714-726. doi: https://doi.org/10.1175/1520-0434(2004)019⟨0714:EOCALA⟩2.0.CO;2

Davies-Jones, R. (2002). Linear and non-linear propagation of supercell storms. *J. Atmos. Sci.*, *59*, 3178-3205.

Dupilka, M. L., & Reuter, G. W. (2006a). Forecasting tornadic thunderstorm potential in Alberta using environmental sounding data. Part II: Helicity, precipitable water, and storm convergence. *Wea. Forecasting*, *21*, 336-346.

Dupilka, M. L., & Reuter, G. W. (2006b). Forecasting tornadic thunderstorm potential in Alberta using environmental sounding data. Part I: Wind shear and buoyancy. *Wea. Forecasting*, *21*, 325-335.

Erfani, A. (1999). *The Winnipeg hailstorm of 16 July 1996: Synoptic analysis and radar observations* (Unpublished master's thesis). University of Alberta, Edmonton, AB. (127 pp)

Erfani, A., Méthot, A., Goodson, R., Bélair, S., Yeh, K.-S., Côte, J., & Moffet, R. (2003). Synoptic and mesoscale study of a severe convective outbreak with the nonhydrostatic Global Environmental Multiscale GEM model. *Meteorol. Atmos. Phys.*, *82*, 386-396. doi: ˚ ¸https://doi.org/10.1007/s00703-001-0585-8

Etkin, D., Brun, S. E., Chrom, S., & Dogra, P. (2002). A tornado scenario for Barrie, Ontario. *Institute for Catastrophic Loss Reduction*.

Fabry, F. (2015). *Radar Meteorology: Principles and Practice.* Cambridge University Press. (272 pp)

Giaiotti, B., & Stel, F. (2007). A multiscale observational case study of an isolated tornadic supercell. *Atmos. Res.*, *83*, 152-161. doi: https://doi.org/10.1016/j.atmosres.2005.08.007

Hanesiak, J., Taszarek, M., Walker, D., Wang, C.-C., & Betancourt, D. (2023). Significant tornado environments in Canada using ERA5-derived convective parameters. *Weather Clim. Extrem.*, *6*.

Helmus, J. J., & Collis, S. M. (2016). *The Python ARM Radar Toolkit (Py-ART), a library for working with weather radar data in the Python programming language.* Retrieved from `https://arm-doe.github.io/pyart/` doi: https://doi.org/10.5334/jors.119

Hersbach, H., Bell, B., Berrisford, P., Hirahara, S., Horányi, A., Muñoz-Sabater, J., . . . Thépaut, J.-N. (2017). *Complete ERA5 from 1940: Fifth generation of ECMWF atmospheric reanalyses of the global climate.* Copernicus Climate Change Service (C3S) Data Store (CDS). doi: https://doi.org/10.24381/cds.143582cf

Hersbach, H., Bell, B., Berrisford, P., Hirahara, S., Horányi, A., Muñoz Sabater, J., . . . Thépaut, J.-N. (2020). The ERA5 global reanalysis. *Quart. J. Roy. Meteor. Soc.*, *146*(730), 1999-2049.

Hobson, J. J. (2011). *Meteorological analysis of the 22 June 2007 F5 tornado in Elie, Manitoba* (Unpublished master's thesis). University of Manitoba, Winnipeg, MB. (133 pp)

Holton, J. R. (2004). *An Introduction to Dynamic Meteorology.* Academic Press. (535 pp)

Hunter, J. D. (2007). Matplotlib: A 2d graphics environment. *Computing in Science and Engineering*, *9*(3), 90-95. doi: https://doi.org/10.1109/MCSE.2007.55

Joe, P., & Dudley, D. (2000). A quick look at the Pine Lake storm. *CMOS Bulletin*, *28*, 172-180.

Joe, P., & May, P. T. (2003). Correction of dual PRF velocity errors for operational Doppler weather radars. *J. Atmos. Ocean. Tech.*, *20*, 429-442.

Johns, R. H., Davies, J. M., & Leftwich, P. W. (1993). Some wind and instability parameters associated with strong and violent tornadoes. Part II: Variations in the combinations of wind and instability parameters. In *The tornado: Its structure, dynamics, prediction, and hazards, geophys. monogr.* (p. 583-590). American Geophysical Union. doi: https://doi.org/10.1029/GM079p0583

Johns, R. H., & Doswell III, C. A. (1992). Severe local storms forecasting. *Wea. Forecasting*, *7*, 588-612. doi: https://doi.org/10.1175/1520-0434(1992)007⟨0588:SLSF⟩2.0.CO;2

Kingsmill, D. E. (1995). Convection initiation associated with a seabreeze front, a gust front, and their collision. *Mon. Wea. Rev.*, *123*, 2913-2933. doi: https://doi.org/10.1175/1520-0493(1995)123,2913:CIAWAS.2.0.CO;2

Klemp, J. B. (1987). Dynamics of tornadic thunderstorms. *Ann. Rev. Fluid Mech.*, *19*, 369-402. doi: https://doi.org/10.1146/annurev.fl.19.010187.002101

Koch, S. E., & Ray, A. (1997). Mesoanalysis of summertime convergence zones in central and eastern north carolina. *Wea. Forecasting*, *12*, 56-77. doi: https://doi.org/10.1175/1520-0434(1997)012,0056:MOSCZI.2.0.CO;2

Kovacs, M., & Kirshbaum, D. J. (2016). Topographic impacts on the spatial distribution of deep convection over southern Québec. *J. Appl. Meteorol. Climatol.*, *55*, 743-762. doi: https://doi.org/10.1175/JAMC-D-15-0239.1

Ladwig, W. (2017). *wrf-python.* Boulder, Colorado. Retrieved from `https://wrf-python.readthedocs.io/en/latest/index.html` doi: https://doi.org/10.5065/D6W094P1

Lascaux, F., Masciadri, E., & Fini, L. (2013). Forecast of surface layer meteorological parameters at Cerro Paranal with a mesoscale atmospherical model. *Mon. Not. R. Astron. Soc.*, *00*, 1-18.

Li, F., Chavas, D. R., Reed, K. A., & II, D. T. D. (2020). Climatology of severe local storm environments and synoptic-scale features over North America in ERA5 reanalysis and CAM6 simulation. *J. Climate*, *33*, 8339-8365.

Li, Q., Xu, J., Liu, X., Yuan, W., & Chen, J. (2016). Characteristics of mesospheric gravity waves over the southeastern Tibetan Plateau region. *J. Geophys. Res.-Space Physics*, *121*, 9204–9221,.

Litta, A. J., Mohanty, U. C., & Bhan, S. C. (2010). Numerical simulation of a tornado over Ludhiana (India) using WRF-NMM model. *Meteorol. Appl.*, *17*, 64-75. doi: https://doi.org/10.1002/met.162

Litta, A. J., Mohanty, U. C., Prasad, S. K., Mohapatra, M., Tyagi, A., & Sahu, S. C. (2012). Simulation of tornado over Orissa (India) on March 31, 2009, using WRF–NMM model. *Nat. Hazards*, *61*, 1219-1242. doi: https://doi.org/10.1007/s11069-011-9979-1

Loken, E. D., Clark, A. J., Xue, M., & Kong, F. (2017). Comparison of next-day probabilistic severe weather forecasts from coarse- and fine-resolution CAMs and a convection-allowing ensemble. *Wea. Forecasting*, *32*, 1403-1421.

Lyons, W. A. (1972). The climatology and prediction of the Chicago lake breeze. *J. Appl. Meteorol.*, *11*, 1259-1270. doi: https://doi.org/10.1175/1520-0450(1972)011⟨1259:TCAPOT⟩2.0.CO;2

Lyons, W. A., & Olsson, L. E. (1973). Detailed mesometeorological studies of air pollution dispersion in the Chicago lake breeze. *Mon. Wea. Rev.*, *101*, 387-403.

MacDonald, J. R., Forbes, G. S., & Marshall, T. P. (2004). The Enhancd Fujita scale [Preprints,]. In *Preprints, 22nd conference on severe local storms.* Hyannis, MA.

Maddox, R. A. (1976). An evaluation of tornado proximity wind and stability data. *Mon. Wea. Rev.*, *104*, 133-142. doi: https://doi.org/10.1175/1520-0493(1976)104⟨0133:AEOTPW⟩2.0.CO;2

Maddox, R. A., Hoxit, L. R., & Chappell, C. F. (1980). A study of tornadic thunderstorm interactions with thermal boundaries. *Mon. Wea. Rev.*, *108*, 322-336. doi: https://doi.org/10.1175/1520-0493(1980)108⟨0322:ASOTTI⟩2.0.CO;2

Mahalik, M. C., Smith, B. R., Elmore, K. L., Kingfield, D. M., Ortega, K. L., & Smith, T. M. (2019). Estimates of gradients in radar moments using a linear least squares derivative technique. *Wea. Forecasting*, *34*, 415-434.

Markowski, P. M., & Richardson, Y. (2010). *Mesoscale Meteorology in Midlatitudes.*

Wiley-Blackwell. (407 pp)

Markowski, P. M., Straka, J. M., Hannon, C., Frame, H., Lancaster, E., Pietrycha, A., … Thompson, R. (2003). Characteristics of vertical wind profiles near supercells obtained from the Rapid Update Cycle. *Wea. Forecasting*, *18*, 1262-1272. doi: https://doi.org/10.1175/1520-0434(2003)018⟨1262:COVWPN⟩2.0.CO;2

Markowski, P. M., Straka, J. M., & Rassmussen, E. N. (2002). Direct surface thermodynamic observations within rear-flank downdrafts of nontornadic and tornadic supercells. *Mon. Wea. Rev.*, *130*, 1692-1721. doi: https://doi.org/10.1175/1520-0493(2002)130⟨1692:DSTOWT⟩2.0.CO;2

Matsangouras, I. T., Nastos, P. T., & Pytharoulis, I. (2011). Synoptic-mesoscale analysis and numerical modeling of a tornado event on 12 February 2010 in northern Greece. *Adv. Sci. Res.*, *6*, 187–194. doi: https://doi.org/10.5194/asr-6-187-2011

Matsangouras, I. T., Nastos, P. T., & Pytharoulis, I. (2016). Study of the tornado event in Greece on March 25, 2009: Synoptic analysis and numerical modeling using modified topography. *Atmos. Res.*, *169*, 566–583. doi: https://doi.org/10.1016/j.atmosres.2015.08.010

May, R. M., Arms, S. C., Marsh, P., Bruning, E., Leeman, J. R., Goebbert, K., … Bruick, Z. S. (2020). *MetPy: A Python Package for Meteorological Data.* Boulder, Colorado. Retrieved from `https://github.com/Unidata/MetPy` doi: https://doi.org/10.5065/D6WW7G29

McCarthy, P. J., Carlsen, D., & Slipec, J. (2008). Elie, Manitoba, Canada, June 22, 2007: Canada's first F5 tornado [Preprints,]. In *Preprints, 24th ams conf. on severe local storms.* Savannah, GA.

McGinley, J. (1982). A diagnosis of Alpine lee cyclogenesis. *Mon. Wea. Rev.*, *110*, 1271-1287.

Miglietta, M. M., Mazon, J., & Rotunno, R. (2017). Numerical simulations of a tornadic supercell over the Mediterranean. *Wea. Forecasting*, *32*, 1209-1226. doi: https://doi.org/10.1175/WAF-D-16-0223.1

Naylor, J., Gilmore, M. S., Thompson, R. L., Edwards, R. E., & Wilhelmson, R. B. (2012). Comparison of objective supercell identification techniques using an idealized cloud model. *Mon. Wea. Rev.*, *140*, 2090-2102.

Palmén, E., & Newton, C. W. (1969). *Atmospheric Circulation Systems.* Academic Press. (603 pp)

Pilguj, N., Taszarek, M., Kryza, M., & Brooks, H. E. (2022). Reconstruction of violent tornado environments in Europe: High-resolution dynamical downscaling of ERA5. *Geophys. Res. Lett.*, *49*. doi: https://doi.org/10.1029/2022GL098242

Pilguj, N., Taszarek, M., Pajurek, L., & Kryza, M. (2019). High-resolution simulation of an isolated tornadic supercell in Poland on 20 June 2016. *Atmos. Res.*, *218*, 145-159. doi: https://doi.org/10.1016/j.atmosres.2018.11.017

Purdom, J. F. W. (1976). Some uses of high-resolution GOES imagery in the mesoscale forecasting of convection and its behavior. *Mon. Wea. Rev.*, *104*, 1474-1483. doi: https://doi.org/10.1175/1520-0493(1976)104,1474:SUOHRG.2.0.CO;2

Python Software Foundation. (2020). *Python v3.8.5.* Retrieved from `https://www.python.org/downloads/release/python-385/`

Rasmussen, E. N., & Blanchard, D. O. (1998). A baseline climatology of sounding-derived supercell and tornado forecast parameters. *Wea. Forecasting*, *13*, 1148-1164. doi: https://doi.org/10.1175/1520-0434(1998)013⟨1148:ABCOSD⟩2.0.CO;2.

Rasmussen, K. L., & Houze Jr., R. A. (2016). Convective initiation near the Andes in subtropical south America. *Mon. Wea. Rev.*, *144*, 2351-2372. doi: https://doi.org/10.1175/MWR-D-15-0058.1

Rotunno, R., & Klemp, J. B. (1982). The influence of the shear-induced pressure gradient on thunderstorm motion. *Mon. Wea. Rev.*, *110*, 133-151.

Sills, D. M. L., Brook, J. R., Levy, I., Makar, P. A., Zhang, J., & Taylor, P. A. (2011). Lake breezes in the southern Great Lakes region and their influence during BAQS-Met 2007. *Atmos. Chem. Phys.*, *11*, 7955–7973.

Sills, D. M. L., & King, P. W. S. (2000). Landspouts at lake breeze fronts in southern Ontario [Preprints,]. In *Preprints, 20th Severe Local Storms Conference.* Orlando, FL.

Sills, D. M. L., Kopp, G. A., Elliott, L., Jaffe, A. L., Sutherland, L., Miller, C. S., ... Wang, W. (2020). The Northern Tornadoes Project - Uncovering Canada's true tornado climatology. *Bull. Amer. Meteor. Soc.*, *101*, E2113-E2132.

Skamarock, W. C., Klemp, J. B., Dudhia, J., Gill, D. O., Liu, Z., Berner, J., ... Huang, X.-Y. (2019). *A description of the Advanced Research WRF model version 4* (Tech. Rep.). NCAR. (NCAR Tech. Note NCAR/TN-556+STR, 162 pp)

Sobash, R. A., Kain, J. S., Bright, D. R., Dean, A. R., Coniglio, M. C., & Weiss, S. J. (2011). Probabilistic forecast guidance for severe thunderstorms based on the identification of extreme phenomena in convection-allowing model forecasts. *Wea. Forecasting*, *26*, 714-728.

Speranza, A. (1975). The formation of baric depressions near the Alps. *Ann. Geophy.*, *28*, 177-217.

Steenburgh, W. J., & Mass, C. F. (1994). The structure and evolution of a Rocky Mountain lee trough. *Mon. Wea. Rev.*, *122*, 2740-2761.

Taszarek, M., Allen, J. T., Pucik, T., Hoogewind, K. A., & Brooks, H. E. (2020). Severe convective storms across Europe and the United States. Part II: ERA5 environments associated with lightning, large hail, severe wind, and tornadoes. *J. Climate*, *33*, 10263-10286. doi: DOI:10.1175/JCLI-D-20-0346.1

Taszarek, M., Czernecki, B., Walczakiewicz, S., Mazur, A., & Kolendowicz, L. (2016). An isolated tornadic supercell of 14 July 2012 in Poland — A prediction technique within the use of coarse-grid WRF simulation. *Atmos. Res.*, *178-179*, 367-379. doi: https://doi.org/10.1016/j.atmosres.2016.04.009

Taszarek, M., Pilguj, N., Allen, J. T., Gensini, V., Brooks, H. E., & Szuster, P. (2021). Comparison of convective parameters derived from ERA5 and MERRA-2 with rawinsonde data over Europe and North America. *J. Climate*, *34*, 3211-3237. doi: https://doi.org/10.1175/JCLI-D-20-0484.1

Thompson, D. B. (2012). *Appalachian lee troughs and their association with severe convective storms* (Unpublished master's thesis). University at Albany, State University of New York, Albany, NY. (152 pp)

Thompson, R. L., Edwards, R., Hart, J. A., Elmore, K. L., & Markowski, P. (2003). Close proximity soundings within supercell environments obtained from the Rapid Update Cycle. *Wea. Forecasting*, *18*, 1243-1261.

Thompson, R. L., Edwards, R., & Mead, C. M. (2004c). An update to the supercell composite and significant tornado parameters [Preprints,]. In *Preprints, 22nd Conference on Severe Local Storms.* Hyannis, MA.

Thompson, R. L., Mead, C. M., & Edwards, R. (2004a). Effective bulk shear in supercell thunderstorm environments [Preprints,]. In *Preprints, 22nd Conference on Severe Local Storms.* Hyannis, MA.

Thompson, R. L., Mead, C. M., & Edwards, R. (2007). Effective storm-relative helicity and bulk shear in supercell thunderstorm environments. *Wea. Forecasting*, *22*, 102-115.

Thompson, R. L., Smith, B. T., Grams, J. S., Dean, A. R., & Broyles, C. (2012). Convective modes for significant severe thunderstorms in the contiguous United States. Part II: Supercell and QLCS tornado environments. *Wea. Forecasting*, *27*, 1136-1154.

Wakimoto, R. M., & Murphey, H. V. (2010). Analysis of convergence boundaries observed during IHOP 2002. *Mon. Wea. Rev.*, *138*, 2737-2760. doi: https://doi.org/10.1175/2010MWR3266.1

Wang, C.-C., & Kirshbaum, D. J. (2015). Thermally forced convection over a mountainous tropical island. *J. Atmos. Sci.*, *72*, 2484-2506.

Weckwerth, T. M., & Parsons, D. B. (2005). A review of convection initiation and motivation for IHOP 2002. *Mon. Wea. Rev.*, *134*, 5-22. doi: https://doi.org/10.1175/MWR3067.1

Weckwerth, T. M., Wilson, J. W., Wakimoto, R. M., & Crook, N. A. (1997). Horizontal convective rolls: Determining the environmental conditions supporting their existence and characteristics. *Mon. Wea. Rev.*, *125*, 505-526.

Weisman, M. K., & Klemp, J. B. (1984). The structure and classification of numerically simulated convective storms in directionally varying wind shears. *Mon. Wea. Rev.*, *112*, 2479-2498.

Weisman, M. K., & Rotunno, R. (2000). The use of vertical wind shear versus helicity in interpreting supercell dynamics. *J. Atmos. Sci.*, *57*, 1452-1472.

Whitaker, J. (2020). *Basemap v.1.2.2.* Retrieved from `https://github.com/matplotlib/basemap/releases`

Wilson, J. W., Trier, S. B., Reif, D. W., Roberts, R. D., & Weckwerth, T. M. (2018). Nocturnal elevated convection initiation of the PECAN 4 July hailstorm. *Mon. Wea. Rev.*, *146*, 243-262. doi: https://doi.org/10.1175/MWR-D-17-0176.1

Wood, R., Stromberg, I. M., & Jonas, P. R. (1999). Aircraft observations of sea-breeze frontal structure. *Quart. J. Roy. Meteor. Soc.*, *125*, 1959-1995.

Yang, Q., & Geerts, B. (2006). Horizontal convective rolls in cold air over water: buoyancy characteristics of coherent plumes detected by an airborne radar. *Mon. Wea. Rev.*, *134*, 2373-2396.

Ziegler, C. L., & Rasmussen, E. N. (1998). The initiation of moist convection at the dryline: Forecasting issues from a case study perspective. *Wea. Forecasting*, *13*, 1106-1131.